



The Infrared Medium-deep Survey. VI. Discovery of Faint Quasars at $z \sim 5$ with a Medium-band-based Approach

Yongjung Kim^{1,2} , Myungshin Im^{1,2} , Yiseul Jeon^{1,3} , Minjin Kim^{4,5} , Soojong Pak^{1,6} , Yoon Chan Taak^{1,2},
Changsu Choi^{1,2}, Jueun Hong^{1,2}, Minhee Hyun^{1,2}, Tae-Geun Ji^{1,6}, Hyunsung David Jun⁷ , Marios Karouzos⁸ ,
Dohyeong Kim^{1,2,9} , Duho Kim¹⁰ , Jae-Woo Kim⁴ , Ji Hoon Kim¹¹ , Hye-In Lee^{1,6}, Seong-Kook Lee^{1,2} , Won-Kee Park⁴,
Yongmin Yoon^{1,2}, Seoyeon Byeon^{1,6}, Sungyong Hwang^{1,2}, Joonho Kim^{1,2}, Sophia Kim^{1,2}, Gu Lim^{1,2}, Insu Paek^{1,2},
Woojin Park^{1,6}, and Suhyun Shin^{1,2}

¹ Center for the Exploration of the Origin of the Universe (CEOEU), Building 45, Seoul National University, 1 Gwanak-ro, Gwanak-gu, Seoul 08826, Republic of Korea; yjkim@astro.snu.ac.kr, mim@astro.snu.ac.kr

² Astronomy Program, FPRD, Department of Physics & Astronomy, Seoul National University, 1 Gwanak-ro, Gwanak-gu, Seoul 08826, Republic of Korea

³ FEROKA Inc., 311-1, 108 Gasandigital2-ro, Geumcheon-gu, Seoul, Republic of Korea

⁴ Korea Astronomy and Space Science Institute, Daejeon 34055, Republic of Korea

⁵ Department of Astronomy and Atmospheric Sciences, College of Natural Sciences, Kyungpook National University, Daegu 41566, Republic of Korea

⁶ School of Space Research, Kyung Hee University, 1732 Deogyong-daero, Giheung-gu, Yongin-si, Gyeonggi-do 17104, Republic of Korea

⁷ Korea Institute for Advanced Study, 85 Hoegi-ro, Dongdaemun-gu, Seoul 02455, Republic of Korea

⁸ Nature Astronomy, Springer Nature, 4 Crinan Street, London N1 9XW, UK

⁹ Kavli Institute for Astronomy and Astrophysics, Peking University, 5 Yi He Yuan Road, Haidian District, Beijing 100871, People's Republic of China

¹⁰ Arizona State University, School of Earth and Space Exploration, P.O. Box 871404, Tempe, AZ 85287-1404, USA

¹¹ Subaru Telescope, National Astronomical Observatory of Japan, 650 North A'ohoku Place, Hilo, HI 96720, USA

Received 2018 July 21; revised 2018 November 17; accepted 2018 November 20; published 2019 January 11

Abstract

The faint quasars with $M_{1450} > -24$ mag are known to hold the key to the determination of the ultraviolet emissivity for the cosmic reionization. But only a few have been identified so far because of the limitations on the survey data. Here we present the first results of the $z \sim 5$ faint quasar survey with the Infrared Medium-deep Survey (IMS), which covers $\sim 100 \text{ deg}^2$ areas in J band to the depths of $J_{\text{AB}} \sim 23$ mag. To improve selection methods, the medium-band follow-up imaging has been carried out using the SED camera for QUasars in Early uNiverse (SQUEAN) on the Otto Struve 2.1 m Telescope. The optical spectra of the candidates were obtained with 8 m class telescopes. We newly discovered 10 quasars with $-25 < M_{1450} < -23$ at $z \sim 5$, among which three have been missed in a previous survey using the same optical data over the same area, implying the necessity for improvements in high-redshift faint quasar selection. We derived photometric redshifts from the medium-band data and found that they have high accuracies of $\langle |\Delta z| / (1 + z) \rangle = 0.016$. The medium-band-based approach allows us to rule out many of the interlopers that contaminate $\gtrsim 20\%$ of the broadband-selected quasar candidates. These results suggest that the medium-band-based approach is a powerful way to identify $z \sim 5$ quasars and measure their redshifts at high accuracy (1%–2%). It is also a cost-effective way to understand the contribution of quasars to the cosmic reionization history.

Key words: cosmology: observations – galaxies: active – galaxies: high-redshift – quasars: supermassive black holes – surveys

1. Introduction

Based on wide-field surveys, half a million quasars have hitherto been discovered (e.g., Pâris et al. 2017), hundreds of them being at a high redshift of $z \gtrsim 5$ (Fan et al. 2001, 2006; Wolf et al. 2003; Richards et al. 2006; Fontanot et al. 2007; Willott et al. 2010; Mortlock et al. 2011; Ikeda et al. 2012, 2017; McGreer et al. 2013, 2018; Venemans et al. 2013, 2015a, 2015b; Bañados et al. 2014, 2016, 2018; Kashikawa et al. 2015; Kim et al. 2015; Jun et al. 2015; Wu et al. 2015; Jiang et al. 2016; Matsuoka et al. 2016; Wang et al. 2016; Yang et al. 2016, 2017; Jeon et al. 2017; Reed et al. 2017). With the identification of high-redshift quasars, we are now broadening our horizon of knowledge deep into the very early universe, especially on the cosmic reionization epoch.

Recent results from the Planck Collaboration (Planck Collaboration et al. 2016) suggest an instantaneous reionization of the intergalactic medium (IGM) at $z \sim 8.8$, which is complete by $z \sim 5$. At $z \sim 2$, we know that active galactic nuclei (AGNs) are the main IGM ionizing sources (e.g., Haardt & Madau 2012), but at higher redshifts, stellar light from low-mass star-forming galaxies has been suggested to be the main reionization source

(Fontanot et al. 2012, 2014; Robertson et al. 2013, 2015; Japelj et al. 2017; Hassan et al. 2018). However, such a scenario has met difficulties: it requires an exceptionally large escape fraction of Lyman continuum photons ($>20\%$ as opposed to a few percent for Lyman break galaxies at $z \sim 3$; Fontanot et al. 2012; Grazian et al. 2017; Japelj et al. 2017; Matthee et al. 2017; Dayal & Ferrara 2018) and/or a very steep faint-end slope for the galaxy luminosity function (LF; Bouwens et al. 2017; Japelj et al. 2017). Alternatively, Giallongo et al. (2015) and Madau & Haardt (2015) suggest that AGNs are the main IGM ionizing sources at $4 < z < 6.5$. However, at $z \sim 6$, results are emerging suggesting that the contribution of faint quasars to the IGM ionization is not significant (e.g., Kim et al. 2015; Onoue et al. 2017). At $z \sim 5$, it is not yet clear whether quasars or galaxies produce more ultraviolet (UV) ionizing photons. The derivation of the LF by Giallongo et al. (2015) relies on the interpolation between a photometric redshift sample of very faint quasar candidates ($M_{1450} > -22$ mag) and spectroscopically identified luminous quasars ($M_{1450} < -26$ mag). With their LF, the major contributor of the UV luminosity density is quasars with $M_{1450} \sim -23.5$ mag.

To date, various groups have performed surveys for $z \sim 5$ quasars with optical and/or infrared data (Ikeda et al. 2012, 2017; McGreer et al. 2013, 2018; Jeon et al. 2016, 2017; Yang et al. 2016, 2017). While most of the spectroscopically identified $z \sim 5$ quasars are bright with $M_{1450} < -24$ mag, the most recent study of McGreer et al. (2018, hereafter M18) focused on the dearth of quasars at $M_{1450} \sim -23$ mag. They found 104 candidates in the Canada–France–Hawaii Telescope Legacy Survey (CFHTLS) stacked images (Gwyn 2012) by using the broadband color selection method and/or the likelihood method, 8 of which are spectroscopically identified as faint quasars ($M_{1450} > -24$ mag) at $4.7 < z < 5.4$. The faint end of the quasar luminosity function (QLF) derived from these quasars shows a lower number density than the result from Giallongo et al. (2015) by an order of magnitude, implying low ionizing emissivity of $z \sim 5$ AGNs and their minor contribution to the cosmic reionization. Recent X-ray studies also suggested that the QLF of Giallongo et al. (2015) could be overestimated and high-redshift AGNs might not be the main contributors to the cosmic reionization (Ricci et al. 2017; Parsa et al. 2018). At the faint end, however, the QLFs from the X-ray AGNs are still higher than those from the UV/optical survey by M18. The selection methods of M18 (both optical color selection and a likelihood method) might miss quasars, or conversely, their candidates could be contaminated by brown dwarfs or galaxies with peculiar colors, considering the lack of near-infrared (NIR) data and the low spectral resolution for using the likelihood method.

Recently, we performed an NIR imaging survey named the Infrared Medium-deep Survey (IMS; M. Im et al. 2018, in preparation), where NIR imaging data were obtained by the United Kingdom Infrared Telescope (UKIRT) in Hawaii. The data reach 5σ depths of $J \sim 23$ mag, over 100 deg^2 areas in the sky, which overlap with the ancillary optical data from CFHTLS, of which 5σ depths reach $\gtrsim 25$ mag in $u'g'r'i'z'$ bands. The combination of these optical and NIR data enables us to sample quasars as faint as $M_{1450} \sim -23$ mag at $z \sim 5$.

In addition to this, we developed the SED Camera for Quasars in EARly uNiverse (SQUEAN; Choi et al. 2015; Kim et al. 2016), as an upgraded instrument of the Camera for Quasars in EARly uNiverse (CQUEAN; Kim et al. 2011; Park et al. 2012; Lim et al. 2013), on the 2.1 m Otto Struve Telescope of McDonald Observatory. This new instrument works with 20 filters consisting of broadband filters (e.g., *griz*) and 50 nm medium bandwidth filters of which the central wavelengths are in the range of 675–1025 nm ($m675\text{--}m1025$ ¹²). Through observations of bright quasars at $z \sim 5$, Jeon et al. (2016) verified its effectiveness in distinguishing high-redshift quasars ($4.7 < z < 6.0$) from brown dwarfs, which are regarded as the main contaminator in high-redshift quasar selection. Furthermore, the redshift determination through the photometric redshift (z_{phot}) derived from broadband and medium-band data shows an accuracy of 1%–2% when compared to the spectroscopic redshift (z_{spec}). Besides, the other surveys with medium-band observations such as COMBO-17 (Wolf et al. 2003), ALHAMBRA (Moles et al. 2008; Matute et al. 2012), and the NEWFIRM Medium-band Survey (van Dokkum et al. 2009) also obtained the redshifts of quasars or galaxies at $1 \lesssim z \lesssim 4$ successfully with few percent uncertainties. In addition, Matute et al. (2013) discovered a

faint quasar with $M_{1450} = -24.07$ mag at $z = 5.41$ from the $\sim 1 \text{ deg}^2$ area of the ALHAMBRA survey by adopting a spectral energy distribution (SED) fitting method (Matute et al. 2012). These results testify the effectiveness of using medium-band observations for the redshift determination of high-redshift quasars.

Based on the optical data of CFHTLS and the NIR data of IMS, we are now performing a $z \sim 5$ quasar survey with a medium-band-based approach to increase the size of the faint quasar sample at $z \sim 5$ and better determine their number density. In this paper, we present the initial results of the $z \sim 5$ quasar survey with the medium-band observations, reporting 10 newly discovered quasars at $z \sim 5$ that are in the magnitude range of $-25 < M_{1450} \text{ (mag)} < -23$. We describe the data we used and the quasar selection method with broadband color criteria in Section 2, while the medium-band-based selection method with imaging follow-up with SQUEAN is described in Section 3. In Section 4, the spectroscopy data we used are characterized, consisting of our spectroscopic observations and supplemental samples from the literature. We present our main results in Section 5: the newly discovered quasars at $z \sim 5$ and the effectiveness of the medium-band observations at finding faint quasars at $z \sim 5$ and measuring their redshift accurately. Finally, we present the implication of the newly discovered quasars to the faint-end slope of the QLF at $z \sim 5$ in Section 6. Throughout the paper, we adopt the cosmological parameters of $\Omega_m = 0.3$, $\Omega_\Lambda = 0.7$, and $H_0 = 70 \text{ km s}^{-1} \text{ Mpc}^{-1}$, which are supported by previous observations (e.g., Im et al. 1997). All magnitudes in this paper are given in the AB system. Note that Vega-based *J*-band magnitudes from IMS were converted to the AB system by following Hewett et al. (2006).

2. Initial Sample Selection

2.1. CFHTLS and IMS Imaging Data

Here we describe the imaging data from which quasar candidates are selected based on the broadband colors. This selection is the initial step of the high-redshift quasar selection, which will be refined later through medium-band imaging follow-up observations (Section 3). The sample selection was first carried out on the optical data from the CFHTLS Wide Survey (Hudelot et al. 2012) and the NIR data from the IMS (M. Im et al. 2018, in preparation) and the Deep eXtragalactic Survey (DXS; Lawrence et al. 2007). There are four extragalactic fields covered by these surveys: XMM-Large Scale Structure survey region (XMM-LSS), CFHTLS Wide survey second region (CFHTLS-W2), Extended Groth Strip (EGS), and Small Selected Area 22h (SA22). Figure 1 shows the positions and layouts of tiles in CFHTLS (black squares), IMS (blue squares), and DXS (purple squares). Hereafter, for convenience, we refer to the combination of NIR data from IMS and DXS as “IMS.”

For CFHTLS, we used stacked images from the TERAPIX processing pipeline (see Hudelot et al. 2012 and the T0007 documentation file¹³), which are given for each CFHTLS tile in each CFHTLS field. Note that “CFHTLS tile” here denotes the $1^\circ \times 1^\circ$ area named from the position of each MegaCam field of view of the Wide survey (e.g., W1+0+0), while “CFHTLS field” indicates the four extragalactic fields of the Wide survey (e.g., W1, W2, W3, and W4). The zero-point (zp) of each tile

¹² The medium-band filters are named as *m* (initial of the medium band) + the central wavelength of the filter in nm.

¹³ <http://terapix.iap.fr/cplt/T0007/doc/T0007-doc.html>

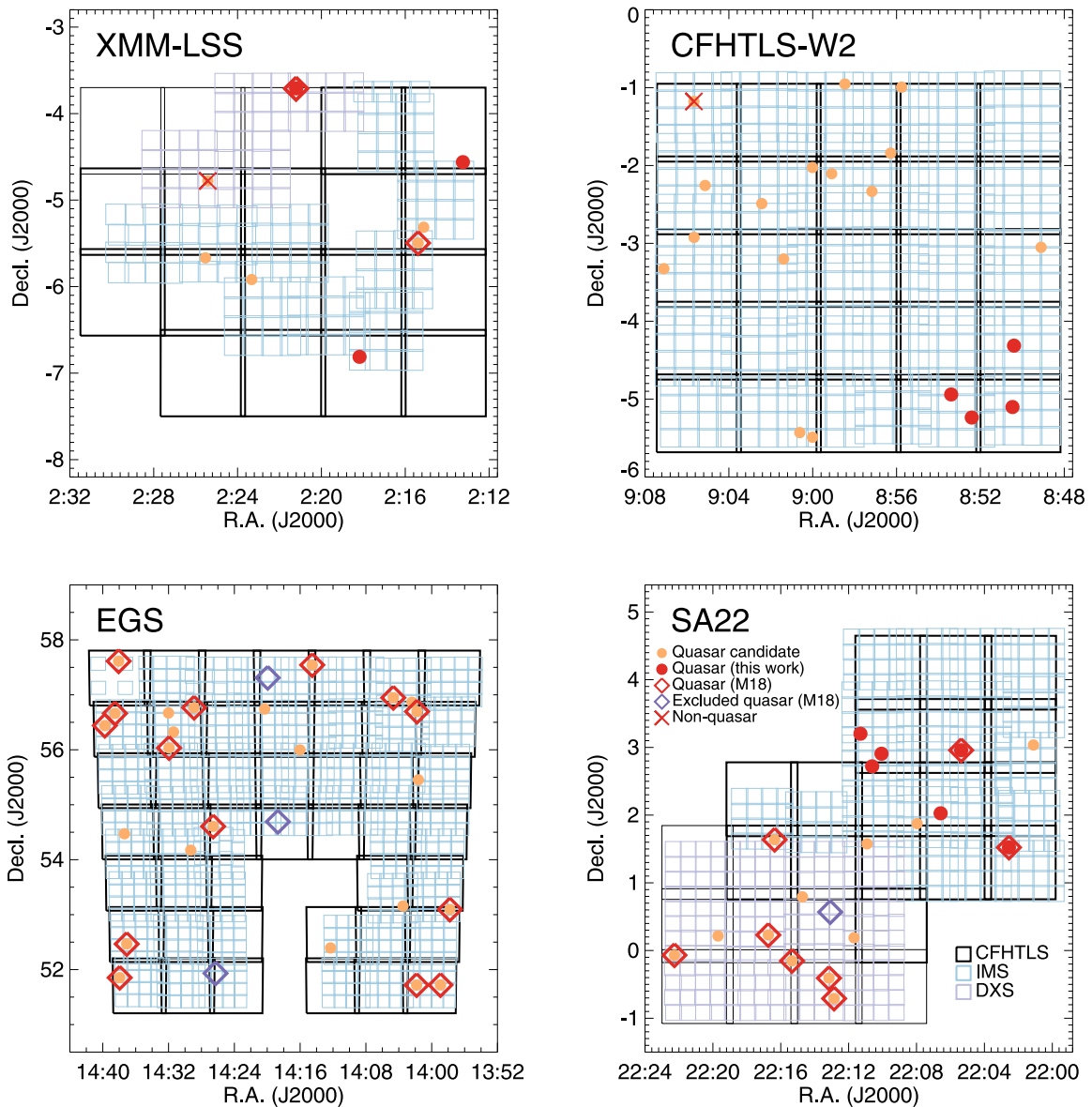


Figure 1. Coverage layout of the high-redshift quasar survey with IMS. The four panels show the different extragalactic fields: XMM-LSS, CFHTLS-W2, EGS, and SA22. The black squares represent the tiles of CFHTLS ($1^\circ \times 1^\circ$ for each), and the blue and purple squares are the tiles of IMS and DXS ($13/65 \times 13/65$ for each), respectively. The total survey areas of CFHTLS, IMS, and DXS in this figure are 103, 73, and 12 deg^2 , respectively. The orange filled circles represent our $z \sim 5$ quasar candidates selected by broadband color criteria, while the spectroscopically identified quasars are additionally marked with the red filled circles (this work) and the red open diamonds (M18). Note that some of the spectroscopically identified quasars with $i < 23$ mag (M18), which are located in our survey area but excluded by our selection owing to their broadband colors, are shown as the purple open diamonds, for easy distinction. The red crosses show the candidates spectroscopically identified as nonquasar objects.

was reestimated by comparing the point sources in CFHTLS with those in Sloan Digital Sky Survey Data Release 12 (SDSS DR12). Through the SQL service of SDSS, we selected point sources, classified as star-like sources, within the appropriate magnitude range of $17 < r < 18.5$, considering the saturation level of CFHTLS and the photometric accuracy (magnitude errors < 0.1 mag) of SDSS data in all the bands. For the position-matched sources with reliable photometry (i.e., spatially isolated point sources without saturation), we compared their auto-magnitudes (MAG_AUTO in SExtractor; Bertin & Arnouts 1996) from CFHTLS with their point-spread function (PSF) magnitudes from SDSS and determined a reliable z_p for each tile. In this process, we converted the auto-magnitudes in optical bands ($u'g'r'i'z'$) into SDSS

photometric systems ($ugriz$), following the transformations from MegaCam to SDSS.¹⁴ For the tiles, which do not overlap with the SDSS area, we used the overlapped stars in adjacent CFHTLS fields. The average and standard deviation of the z_p value offsets in u , g , r , i , and z bands are 0.14 ± 0.04 mag, -0.06 ± 0.02 mag, -0.05 ± 0.02 mag, -0.06 ± 0.02 mag, and -0.09 ± 0.03 mag, respectively.

On the other hand, for IMS, we stacked the images of each detector covering the area of $13/65 \times 13/65$ instead of stacking the images of each IMS tile covering the $0.75 \times 0.75 \text{ deg}^2$ area, in order to determine a reliable z_p for each image. The z_p of each stacked image was scaled to 28.0 in the Vega system by

¹⁴ <http://www.cadc-ccda.hia-ihp.nrc-cnrc.gc.ca/en/megapipeline/docs/filtold.html>

comparing the J -band auto-magnitudes of point sources in IMS and those from the Two Micron All Sky Survey (2MASS) catalog (Skrutskie et al. 2006). The average 5σ point-source detection limits of the optical/NIR images are $u = 26.1$ mag, $g = 26.4$ mag, $r = 25.9$ mag, $i = 25.6$ mag, $z = 24.6$ mag, and $J = 22.9$ mag¹⁵, enabling us to select $z \sim 5$ quasars with $i \lesssim 23$ mag or those as faint as $M_{1450} \lesssim -23$ mag. For photometry, we detected sources in the i' -band images and estimated fluxes in each band within $2 \times \text{FWHM}_{i'}$ diameters, using the dual-image mode of the SExtractor software, with DETECT_THRESH of 1.3 and DETECT_MINAREA of 9, corresponding to a $\sim 4\sigma$ detection limit. By applying aperture correction factors derived from bright stars in each filter image, we converted the aperture magnitudes to total magnitudes. Note that the total magnitudes were also converted to the SDSS photometric system.

Although we adjusted the z_p values of the optical/NIR images with point sources in the SDSS/2MASS catalogs, respectively, there are small inconsistencies of stellar loci on the order of $\lesssim 0.1$ mag on color-color diagrams from tile to tile. Compared to the stellar libraries of Pickles (1998), these offsets were already reported by the TERAPIX team as one can see in their color-color diagrams (see footnote 13). Since the color offset can affect the quasar candidate selection substantially, we calculated the color offsets of stellar loci in each CFHTLS tile to correct the inconsistencies and improve the color selection for quasar candidates (see details in Appendix A). Note that the color offsets are not adjusted for the apparent magnitudes of the quasars in this paper, but are used only for the color selection of quasar candidates in Section 2.2.

For the Galactic extinction correction, we used the extinction map of Schlafly & Finkbeiner (2011) with the Cardelli et al. (1989) law assuming $R_V = 3.1$. To account for the pixel-to-pixel correlation from the image-combining process, we scaled magnitude errors accordingly, using the noise properties (σ_N) of an effective aperture size N in each image (Gawiser et al. 2006; Jeon et al. 2010; Kim et al. 2015).

2.2. Broadband Color Selection

The broadband color selection follows the criteria of McGreer et al. (2013), where they defined the color selection by simulating the color tracks using low-redshift SDSS quasar spectra that are redshifted to $z \sim 5$. Considering the deeper depths of CFHTLS and IMS, we made a minor change to the i -magnitude limit. The following shows the selection criteria that we used:

1. $i < 23$,
2. $S/N(u) < 2.5$,
3. $g-r > 1.8$ or $S/N(g) < 3.0$,
4. $r-i > 1.2$,
5. $i-z < 0.625 ((r-i) - 1.0)$,
6. $i-z < 0.55$,
7. $i - J < ((r-i) - 1.0) + 0.56$,

where the signal-to-noise ratio (S/N) values are directly estimated from the fluxes and flux errors in the aperture mentioned above. The candidates satisfying the criteria were

visually inspected to exclude spurious objects such as cross-talks, diffraction spikes, etc., resulting in 70 $z \sim 5$ quasar candidates. The positions of the candidates (orange circles) are plotted on the layouts in Figure 1. Figure 2 shows the color-color diagrams ($g-r$ versus $r-i$, $r-i$ versus $i-z$, and $r-i$ versus $i-J$) of objects in the multiband catalog and the broadband color selection criteria (the black solid lines). The broadband photometries of our candidates are listed in Table 1. In this paper, we only include the candidates that are spectroscopically observed in this work or previous works (e.g., M18) and also observed in medium bands, instead of the full sample of our candidates (see details of the spectroscopic sample in Section 4).

3. Medium-band Selection

3.1. Medium-band Observation

To further exclude interlopers and better determine redshifts photometrically, we observed our candidates in medium bands with SQUEAN from 2015 December to 2018 April. Since the Lyman-alpha ($\text{Ly}\alpha$; 1216 Å) break of a $z \sim 5$ quasar is expected to be located at $\lambda_{\text{obs}} \sim 7300$ Å, the medium-band observations were performed mainly with the $m725$ and $m775$ filters. If the two medium-band data were not enough to identify the object as a $z > 5.1$ quasar (i.e., $m725 - m775 < 1$; see Section 3.2), additional imaging data in the $m675$ band were also obtained. For the spectroscopically identified quasars, if needed, observations in the $m675$ and/or $m825$ bands were also carried out to check the accuracy of the z_{phot} from medium-band data. For each band, we took 3–70 frames with exposure times of 1–3 minutes, which gives the total integration time of 0.05–1.75 hr per band per filter. Note that brighter candidates ($i < 22$ mag) were observed as high-priority targets, when the observing condition was unstable with a seeing size of $> 1''.2$. Among the 70 quasar candidates, 58 candidates were observed in the $m725$ and $m775$ bands, and 45 of them were further observed in the $m675$ band.

We reduced the medium-band data, following the procedure in Jeon et al. (2016). After subtracting the bias and dark frames, we divided the science frames by the normalized flat frames, which were produced from the twilight sky. Excluding the images taken under bad weather conditions (e.g., low signals due to heavy clouds), the science images after the reduction were combined. We first detected the sources in the combined images with a detection threshold of $\sim 2.7\sigma$ (DETECT_THRESH of 1.2 and DETECT_MINAREA of 5). The z_p of each medium-band image was determined by fitting the stellar templates to the broadband photometry (riz) of stars in each field (see details in Jeon et al. 2016). Note that we regarded auto-magnitudes of the stars in each medium band as total magnitudes for the z_p determination. The uncertainty in the z_p determination is found to be ~ 0.03 mag, by taking the standard deviation of the z_p values from the stars in the same field. For each quasar candidate, we estimated the aperture magnitude (size of $2 \times \text{FWHM}_{\text{mb}}$ is used, where FWHM_{mb} is FWHM of point sources in each medium-band image) with forced photometry on the target position determined in the i -band image. We applied the aperture correction factor determined from the stars in each field. Like the broadband photometry, the Galactic extinction was corrected by following the Cardelli et al. (1989) law assuming $R_V = 3.1$ with the extinction map of Schlafly & Finkbeiner (2011), and we also scaled the

¹⁵ Unlike the homogeneous optical data, the J -band data including IMS and DXS are inhomogeneous. The average depths of four extragalactic fields of IMS (XMM-LSS, CFHTLS-W2, EGS, and SA22) are 23.2, 22.7, 22.7, and 23.2 mag, respectively, and those of DXS (XMM-LSS and SA22) are 23.7 and 23.9 mag, respectively.

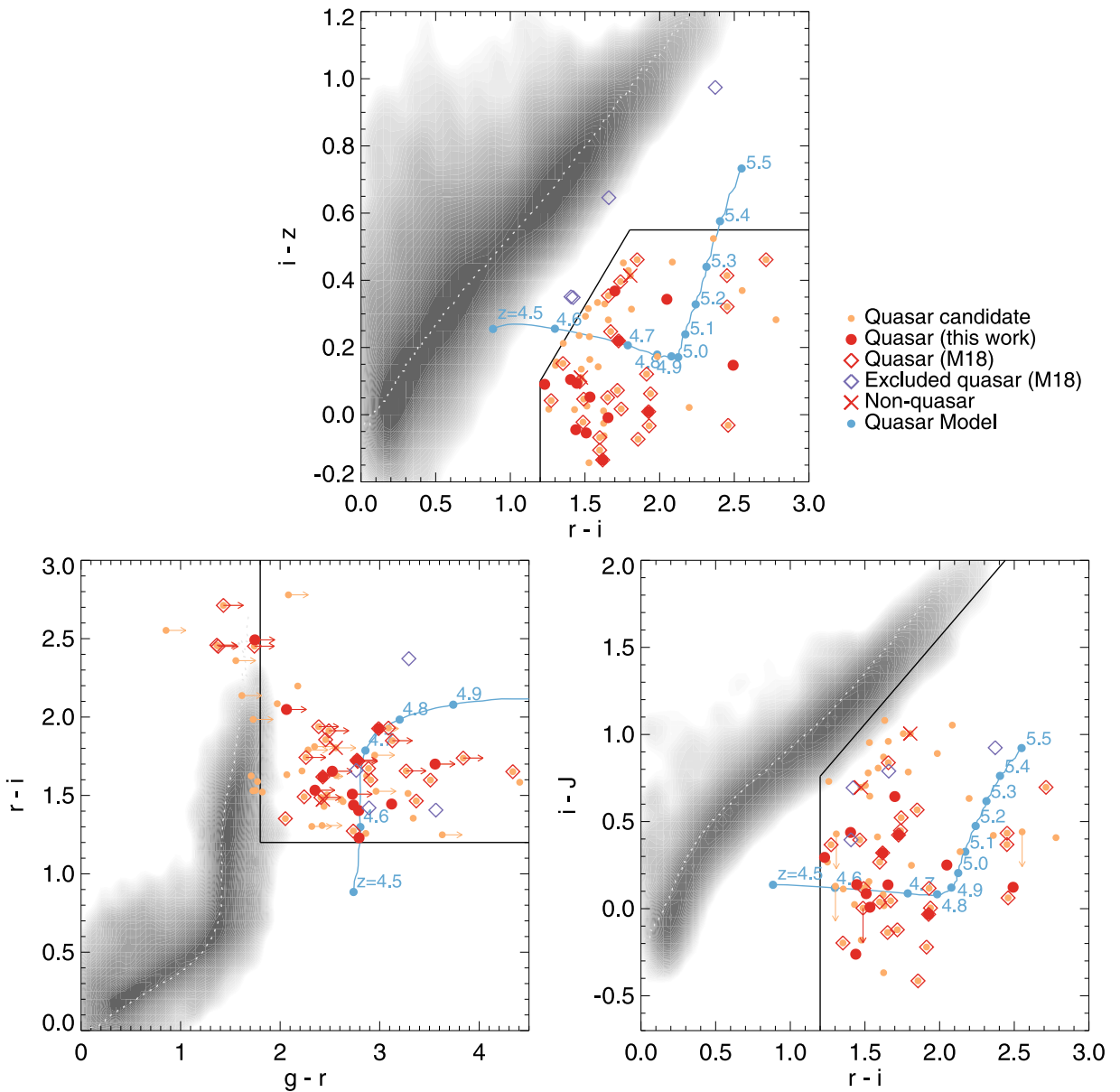


Figure 2. Color-color diagrams for quasar selection. The gray contours represent the point sources from one of the tiles of CFHTLS (and IMS), while the dotted lines on the contours indicate the stellar loci of Covey et al. (2007). The black solid lines indicate our selection criteria, and the blue filled circles with lines show the redshift evolution of our quasar SED model described in Section 5.3.1 on the color-color spaces. The other symbols of candidates, quasars, and nonquasars are the same as in Figure 1. Note that the arrows indicate the upper/lower limit of colors.

SEXTRACTOR-derived magnitude errors to account for the correlated noise in the stacked image (σ_N). We gave the upper limit, which is defined as the magnitude limit for the 2.7σ detection, to the objects with no detection or magnitudes less than the upper limit. The observing runs and the medium-band photometry are given in Table 2. As with Table 1, only the spectroscopically examined candidates are listed.

3.2. Medium-band Selection of $z \sim 5$ Quasar Candidates

Figure 3 shows the color-color diagrams for the medium bands only (top panel for $m675-m725$ versus $m725-m775$) and for the combinations of broad- and medium-band colors (bottom panels for $r-i$ versus $m675-m725$ and $r-i$ versus $m725-m775$, respectively). The gray filled circles represent the colors of the 175 star templates covering various spectral types and luminosity

classes (Gunn & Stryker 1983) and the 41 L/T dwarf star models (Burrows et al. 2006). The other symbols are identical to those in Figure 2. We followed the color selection criteria with medium bands suggested by Jeon et al. (2016):

1. $m675 - m725 > 1$ and $m675 - m725 > m725 - m775 + 1.5$ ($4.7 < z < 5.1$),
2. $m725 - m775 > 1$ ($5.1 < z < 5.5$),

which are plotted as dotted lines in Figure 3. The top panel in the figure shows the above criteria at a glance. Among 45 candidates observed in the $m675$, $m725$, and $m775$ bands, 33 candidates satisfy the above color selection criteria. The medium-band color criteria ($m675 - m725 > 1$ and $m725 - m775 > 1$) could be roughly adopted to the combination of broad- and medium-band colors (dashed lines). Note that the former criterion is limited by $r-i$ color: $m675 - m725 > 0.5 (r-i) - 0.25$.

Table 1
Broadband Photometry of Spectroscopically Observed Quasar Candidates

ID	R.A. (J2000)	Decl. (J2000)	<i>u</i> (mag)	<i>g</i> (mag)	<i>r</i> (mag)	<i>i</i> (mag)	<i>z</i> (mag)	<i>J</i> (mag)
Spectroscopically Identified Quasars								
IMS J021315–043341 ^{a,b}	02:13:15.00	–04:33:40.5	>26.70	>26.59	24.01 ± 0.09	22.35 ± 0.02	22.28 ± 0.06	22.41 ± 0.12
IMS J021523–052946	02:15:23.29	–05:29:45.9	>26.46	>26.57	22.71 ± 0.02	20.99 ± 0.01	20.53 ± 0.01	20.75 ± 0.02
IMS J021811–064843 ^{a,b}	02:18:10.80	–06:48:42.6	>26.73	25.70 ± 0.13	22.87 ± 0.02	21.46 ± 0.01	21.20 ± 0.04	21.14 ± 0.04
IMS J022112–034232 ^a	02:21:12.32	–03:42:31.8	>26.80	26.44 ± 0.32	23.41 ± 0.09	21.48 ± 0.01	21.38 ± 0.03	21.72 ± 0.10
IMS J022113–034252	02:21:12.62	–03:42:52.3	>26.80	24.57 ± 0.06	21.02 ± 0.01	19.41 ± 0.00	19.43 ± 0.01	19.58 ± 0.03
IMS J085024–041850 ^{a,b}	08:50:23.81	–04:18:49.6	>26.31	26.07 ± 0.13	23.31 ± 0.03	21.90 ± 0.01	21.89 ± 0.04	22.29 ± 0.17
IMS J085028–050607 ^{a,b}	08:50:28.16	–05:06:06.9	>26.21	>26.75	24.67 ± 0.14	22.66 ± 0.02	22.34 ± 0.06	22.52 ± 0.28
IMS J085225–051413 ^{a,b}	08:52:24.73	–05:14:13.4	>26.59	>26.50	24.15 ± 0.09	22.64 ± 0.02	22.61 ± 0.06	22.75 ± 0.26
IMS J085324–045626 ^{a,b}	08:53:23.68	–04:56:25.6	>26.53	>26.48	23.75 ± 0.08	22.27 ± 0.02	22.35 ± 0.06	22.30 ± 0.11
IMS J135747+530543	13:57:47.34	+53:05:42.6	>26.31	>26.19	23.09 ± 0.04	21.21 ± 0.01	20.72 ± 0.02	20.83 ± 0.03
IMS J135856+514317	13:58:55.96	+51:43:17.0	>26.66	26.37 ± 0.19	21.99 ± 0.02	20.40 ± 0.00	20.29 ± 0.01	20.77 ± 0.03
IMS J140147+564145	14:01:46.97	+56:41:44.8	>26.50	26.63 ± 0.20	23.54 ± 0.05	21.67 ± 0.01	21.60 ± 0.04	21.71 ± 0.07
IMS J140150+514310	14:01:49.96	+51:43:10.4	>26.72	>26.73	25.33 ± 0.13	22.93 ± 0.03	22.90 ± 0.07	23.10 ± 0.22
IMS J140440+565651	14:04:40.29	+56:56:50.7	>26.89	24.62 ± 0.05	22.36 ± 0.01	20.94 ± 0.00	20.86 ± 0.01	20.99 ± 0.03
IMS J141432+573234	14:14:31.56	+57:32:34.4	>26.85	>26.67	23.45 ± 0.05	21.81 ± 0.01	21.42 ± 0.03	21.18 ± 0.11
IMS J142635+543623	14:26:34.86	+54:36:22.7	>26.86	24.41 ± 0.04	21.51 ± 0.01	19.92 ± 0.00	19.89 ± 0.01	19.78 ± 0.02
IMS J142854+564602	14:28:53.85	+56:46:02.0	>27.13	26.64 ± 0.30	23.75 ± 0.05	22.07 ± 0.01	21.75 ± 0.04	22.26 ± 0.15
IMS J143156+560201	14:31:56.36	+56:02:00.9	>27.16	24.76 ± 0.06	22.01 ± 0.01	20.74 ± 0.00	20.62 ± 0.02	20.60 ± 0.04
IMS J143705+522801	14:37:05.17	+52:28:00.8	>26.75	>26.69	24.20 ± 0.08	22.30 ± 0.02	22.10 ± 0.04	22.75 ± 0.16
IMS J143757+515115	14:37:56.54	+51:51:15.1	>26.90	>26.68	24.91 ± 0.07	22.43 ± 0.03	22.07 ± 0.05	22.20 ± 0.12
IMS J143804+573646	14:38:04.05	+57:36:46.4	>26.56	>26.49	24.08 ± 0.07	22.60 ± 0.02	22.61 ± 0.04	>22.86
IMS J143831+563946	14:38:30.83	+56:39:46.4	>26.49	25.01 ± 0.09	22.98 ± 0.03	21.56 ± 0.01	21.39 ± 0.04	22.03 ± 0.15
IMS J143945+562627	14:39:44.88	+56:26:26.6	>26.60	>26.72	24.48 ± 0.09	22.67 ± 0.03	22.63 ± 0.10	22.42 ± 0.23
IMS J220233+013120 ^a	22:02:33.20	+01:31:20.3	>26.53	>26.84	24.02 ± 0.07	22.26 ± 0.03	21.95 ± 0.04	22.02 ± 0.08
IMS J220522+025730 ^a	22:05:22.15	+02:57:30.0	>26.47	25.80 ± 0.13	23.32 ± 0.05	21.66 ± 0.01	21.68 ± 0.05	21.43 ± 0.08
IMS J220635+020136 ^{a,b}	22:06:34.81	+02:01:36.3	>26.06	>26.31	24.58 ± 0.04	22.08 ± 0.02	21.81 ± 0.05	22.08 ± 0.10
IMS J221004+025424 ^{a,b}	22:10:03.90	+02:54:24.4	>26.65	26.37 ± 0.15	23.56 ± 0.06	22.36 ± 0.01	22.30 ± 0.05	22.19 ± 0.08
IMS J221037+024314 ^{a,b}	22:10:36.99	+02:43:13.7	>26.60	>26.71	23.13 ± 0.04	21.46 ± 0.00	21.12 ± 0.02	20.95 ± 0.03
IMS J221118+031207 ^{a,b}	22:11:18.37	+03:12:07.4	>26.71	25.91 ± 0.09	22.77 ± 0.02	21.36 ± 0.00	21.29 ± 0.02	21.35 ± 0.04
IMS J221251–004231	22:12:51.49	–00:42:30.7	>26.78	24.33 ± 0.04	21.77 ± 0.01	19.91 ± 0.00	19.89 ± 0.00	20.48 ± 0.04
IMS J221310–002428	22:13:09.67	–00:24:28.1	>26.88	>27.08	24.59 ± 0.15	22.65 ± 0.02	22.49 ± 0.05	22.80 ± 0.21
IMS J221520–000908	22:15:20.22	–00:09:08.4	>26.54	>26.52	25.05 ± 0.09	22.19 ± 0.03	21.77 ± 0.05	21.67 ± 0.07
IMS J221622+013815	22:16:21.85	+01:38:14.7	>26.42	>26.73	25.32 ± 0.11	22.85 ± 0.03	22.35 ± 0.05	22.63 ± 0.12
IMS J221644+001348	22:16:44.02	+00:13:48.2	>26.40	25.48 ± 0.16	22.07 ± 0.01	20.54 ± 0.00	20.34 ± 0.01	20.26 ± 0.04
IMS J222216–000406	22:22:16.02	–00:04:05.7	>26.28	>26.60	23.78 ± 0.06	22.02 ± 0.01	21.83 ± 0.04	22.26 ± 0.11
Spectroscopically Identified Nonquasars								
IMS J022525–044642	02:25:25.18	–04:46:41.5	>26.85	>26.70	24.27 ± 0.12	22.85 ± 0.04	22.64 ± 0.10	22.37 ± 0.17
IMS J090540–011038	09:05:40.10	–01:10:38.4	>26.80	>26.58	24.02 ± 0.07	22.20 ± 0.02	21.68 ± 0.04	21.34 ± 0.10

Notes. All magnitudes are given in the AB system, and their errors are scaled with σ_N , the noise properties of an effective aperture size N (see details in Section 2.1). Note that all the magnitudes are not corrected with C_s^{offset} (see also Section 2.1 and Appendix A).

^a These quasars are spectroscopically observed in this work.

^b These quasars are newly discovered in this work, while others are discovered by previous studies (McGreer et al. 2013; M18; Ikeda et al. 2017).

4. Spectroscopy Data

We performed spectroscopic observations of 15 candidates from the broadband selection method, among which 10 satisfy the medium-band selection. The medium-band-selected candidates were spectroscopically observed prior to other candidates. Here “other candidates” mean the objects that are outside the medium-band selection boxes but could be included considering their large magnitude uncertainties (or upper limits of flux at short wavelength). These observations are reported below in Table 3. Additionally, we took spectra of seven candidates from the broadband photometry, *before* we improved the photometry as described in Section 2.1. After improving the photometry as described in Section 2.1, they turned out not to satisfy the broadband quasar selection criteria, and they are all found to be nonquasars from spectroscopy. For completeness,

we present these nonquasar spectra in Appendix B, but we will exclude them in our analysis hereafter. Additionally, we used published redshifts for some of the medium-band observed objects, as described in Section 4.3.

4.1. Gemini/GMOS Observation

Spectroscopic observations of 13 candidates were carried out with Gemini Multi-Object Spectrographs (GMOS; Hook et al. 2004) on Gemini-North and Gemini-South 8 m Telescopes at Maunakea, Hawaii, and Cerro Pachon, Chile, respectively, on 2016 September 3–8 (PID: GS-2016B-Q-46), 2018 March 20 and June 18 (PID: GS-2018A-Q-220), and 2018 May 18 (PID: GN-2018A-Q-315). The sky was almost clear, with average seeing of $\sim 1''$. To ease the sky subtraction for the faint targets, the Nod & Shuffle (N&S) observing mode was adopted

Table 2
Medium-band Photometry of Spectroscopically Observed Quasar Candidates

ID	Observing Runs, Exposure Times (s), and Magnitudes (mag)											
	<i>m</i> 675			<i>m</i> 725			<i>m</i> 775			<i>m</i> 825		
Spectroscopically Identified Quasars												
IMS J021315–043341	Oct 17	3600	>23.82	Oct 15	1800	22.59 ± 0.17	Oct 15	4140	23.43 ± 0.80	Oct 17	2700	22.86 ± 0.26
IMS J021523–052946	Dec 17	1800	>22.33	Dec 17	1800	>22.54	Dec 17	1260	20.77 ± 0.23
IMS J021811–064843	Oct 17	1800	22.92 ± 0.17	Feb 16	900	21.25 ± 0.13	Feb 16	900	21.70 ± 0.27	Oct 17	1800	21.57 ± 0.07
IMS J022112–034232	Sep 17	1800	22.97 ± 0.54	Feb 16	900	21.27 ± 0.08	Feb 16	900	21.90 ± 0.28	Sep 17	1800	21.79 ± 0.22
IMS J022113–034252	Dec 17	600	21.27 ± 0.17	Dec 17	300	19.33 ± 0.04	Dec 17	300	19.92 ± 0.06
IMS J085024–041850	Dec 17	2700	23.67 ± 0.73	Dec 17	1800	21.94 ± 0.11	Dec 17	1800	23.07 ± 0.34
IMS J085028–050607	Apr 17	3600	>23.97	Apr 17	3600	21.78 ± 0.10	Apr 18	3600	22.63 ± 0.16
IMS J085225–051413	Apr 18	3600	>24.03	Apr 17	3600	22.53 ± 0.10	Apr 17	3600	23.02 ± 0.26
IMS J085324–045626	Dec 17	3240	24.25 ± 0.60	Feb 16	1800	22.37 ± 0.15	Feb 16	1800	23.03 ± 0.40
IMS J135747+530543	Jan 18	2700	22.47 ± 0.34	Apr 17	3600	23.08 ± 0.20	Apr 17	3600	20.53 ± 0.08	Dec 17	900	21.22 ± 0.12
IMS J135856+514317	Feb 17	900	22.37 ± 0.12	Feb 16	900	20.55 ± 0.05	Feb 16	900	20.86 ± 0.09
IMS J140147+564145	Feb 17	1800	22.82 ± 0.19	Feb 16	900	20.88 ± 0.04	Feb 16	960	21.46 ± 0.08
IMS J140150+514310	Apr 17	3600	24.12 ± 0.35	Apr 17	3600	22.28 ± 0.15	Apr 18	3600	23.19 ± 0.22
IMS J140440+565651	Dec 17	3540	23.24 ± 0.40	Apr 17	900	21.38 ± 0.06	Apr 17	1440	21.70 ± 0.09	16Apr	900	21.61 ± 0.09
IMS J141432+573234	Feb 17	3600	23.20 ± 0.18	Feb 16	900	22.75 ± 0.23	Feb 16	900	21.25 ± 0.10	Dec 17	1620	22.12 ± 0.20
IMS J142635+543623	Dec 17	300	21.86 ± 0.19	Dec 17	180	19.64 ± 0.04	Dec 17	180	20.09 ± 0.06	Dec 17	180	20.06 ± 0.07
IMS J142854+564602	Dec 17	2700	>23.89	Apr 17	4140	22.63 ± 0.15	Apr 17	1800	22.94 ± 0.36
IMS J143156+560201	Feb 17	900	22.99 ± 0.30	Apr 17	1800	21.09 ± 0.11	Apr 17	2340	21.14 ± 0.20	16Apr	900	21.04 ± 0.06
IMS J143705+522801	Dec 17	2700	>23.78	Dec 17	900	22.14 ± 0.12	Dec 17	1800	22.91 ± 0.28
IMS J143757+515115	Feb 18	2700	>23.57	Apr 17	3600	>23.88	Apr 17	1800	22.63 ± 0.34	Feb 18	1980	22.97 ± 0.42
IMS J143804+573646	Dec 17	2700	>23.70	Apr 17	4140	22.61 ± 0.17	Apr 17	5400	23.10 ± 0.61	Apr 18	2040	22.86 ± 0.33
IMS J143831+563946	Feb 17	6300	>23.39	Jun 16	900	21.33 ± 0.14	Jun 16	900	22.03 ± 0.22	Apr 18	1260	22.04 ± 0.22
IMS J143945+562627	Dec 17	2700	23.51 ± 0.30	Apr 17	4500	22.59 ± 0.15	Apr 17	1800	23.62 ± 0.97
IMS J220233+013120	Dec 16	3060	>23.18	Oct 15	2160	>23.67	Oct 15	2160	22.22 ± 0.11	Dec 16	1800	>22.17
IMS J220522+025730	Jul 16	900	>22.73	Oct 15	1260	21.69 ± 0.07	Oct 15	1260	21.74 ± 0.09	Dec 16	900	22.32 ± 0.31
IMS J220635+020136	Dec 16	1620	>22.53	Jun 16	1980	22.07 ± 0.17	Jun 16	1800	21.88 ± 0.18	Oct 17	1800	22.04 ± 0.11
IMS J221004+025424	Dec 16	4200	22.36 ± 0.27	Oct 15	1800	22.85 ± 0.20	Oct 15	1800	22.72 ± 0.19	Dec 16	1800	23.33 ± 0.56
IMS J221037+024314	Dec 16	1860	22.67 ± 0.49	Oct 15	2520	23.12 ± 0.41	Oct 15	1620	21.17 ± 0.08	Oct 17	2520	21.36 ± 0.06
IMS J221118+031207	Jul 16	900	23.10 ± 0.38	Oct 15	1800	21.51 ± 0.11	Oct 15	1800	22.07 ± 0.20	Dec 16	1440	21.77 ± 0.18
IMS J221251–004231	Dec 17	600	22.48 ± 0.37	Dec 17	300	19.73 ± 0.06	Dec 17	600	20.54 ± 0.12
IMS J221310–002428	Oct 17	5400	24.07 ± 0.37	Jun 16	3600	22.24 ± 0.14	Jun 16	3600	22.91 ± 0.35	Oct 17	4320	22.94 ± 0.22
IMS J221520–000908	Oct 17	5040	>23.51	Oct 15	1800	>23.40	Oct 15	1800	21.37 ± 0.10	Oct 17	2700	21.94 ± 0.14
IMS J221622+013815	Oct 17	5400	>24.57	Oct 15	3780	22.72 ± 0.13	Oct 15	3600	22.89 ± 0.22	Oct 17	3600	22.89 ± 0.18
IMS J221644+001348	Dec 17	1560	22.37 ± 0.37	Dec 17	540	20.27 ± 0.07	Dec 17	600	20.40 ± 0.12
IMS J222216–000406	Dec 17	1080	21.65 ± 0.23	Jan 18	900	>21.46
Spectroscopically Identified Nonquasars												
IMS J022525–044642	Oct 17	3600	>23.46	Oct 15	3600	23.66 ± 0.31	Oct 15	3420	23.22 ± 0.30
IMS J090540–011038	Apr 17	3600	21.93 ± 0.20	Apr 17	3600	21.90 ± 0.33

Note. All magnitudes are given in the AB system, and their errors are scaled with σ_M .

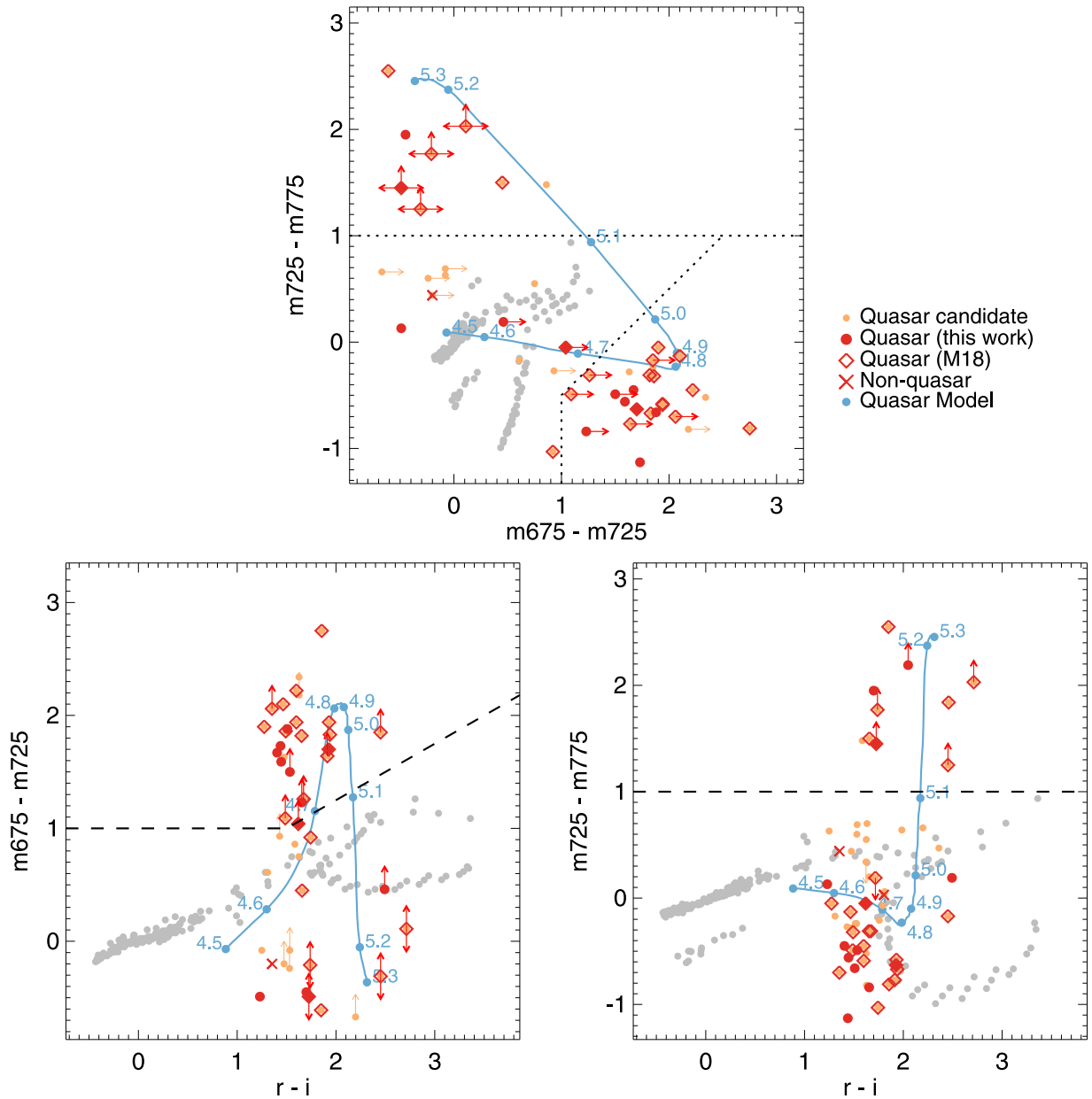


Figure 3. Medium-band colors of quasars. The symbols of candidates, quasars, nonquasars, and the quasar model are the same as in Figure 2. The gray filled circles represent the colors of typical stars from stellar templates of main sequence (Gunn & Stryker 1983) and dwarf (Burrows et al. 2006). The dotted lines are the medium-band selection criteria provided by Jeon et al. (2016), while the dashed lines are the additional criteria presented in this work.

with a $1''$ width N&S slit. The spectra were obtained by using the R150+_G5326 grating, which has a resolution of $R \sim 315$ at 717 nm for a slit width of $1''$, and the GG455_G0329 or OG515_G0330 filters to avoid the zeroth-order overlap. This setup gives the wavelength range of 4550 or 5150–10300 Å. In order to cover the gaps between the chips on the Hamamatsu CCD, the central wavelengths were set to 7100 and 7250 Å. This setting allows the detection of the redshifted Ly α break, which is expected to be located at ~ 7200 Å for $z \sim 5$ quasars. For the observing run in the 2018A semester, we set the central wavelengths to 4300 and 4600 Å for the Gemini-South, in order to avoid the bad columns on the CCD, and 6350 and 6650 Å for the Gemini-North. Note that we adopted a 4×4 binning in spatial/spectral pixels to maximize the S/N.

For one target, IMS J221046+024313, we obtained its spectrum through the MOS observing mode of GMOS-S (PID:

GS-2016B-Q-11), during which we observed other targets of interest for another program. For the MOS observation with the N&S mode, we used the same R150+_G5326 grating with the RG610_G0331 filter, and the central wavelengths were set to 8900 and 9000 Å. To increase the S/N, the spectrum was also binned with 4×4 .

For data reduction, the spectra were processed by using the Gemini IRAF package. After the bias subtraction and flat-fielding, sky lines were subtracted with the shuffled spectra. The wavelength calibration was done with CuAr arc lines, and the flux calibration was done with standard stars (LTT 7379, CD 329927, and Wolf 1346). For IMS J221036 + 024313 with the MOS observation, the wavelength calibration preceded the sky subtraction owing to the alignments of sky lines in the spatial direction. The aperture size for the spectral extraction was set at $1''$ in diameter for all cases. Note that the

Table 3
Spectroscopic Observations of $z \sim 5$ Quasar Candidates

ID	Telescope/Instrument	Date	Exposure Time (s)	Seeing (arcsec)
Spectroscopically Identified Quasars				
IMS J021315–043341	<i>Magellan</i> /IMACS	2016 Dec 4–5	4500	0.5–0.8
IMS J021811–064843	Gemini/GMOS-S	2016 Sep 6	480	1.0–1.1
IMS J022112–034232	Gemini/GMOS-S	2016 Sep 3	960	1.2–1.3
IMS J085024–041840	Gemini/GMOS-N	2018 May 18	1440	0.7
IMS J085028–050607	Gemini/GMOS-S	2018 Mar 20	3000	1.1
IMS J085225–051413	Gemini/GMOS-S	2018 Mar 20	3000	1.1
IMS J085324–045626	<i>Magellan</i> /IMACS	2016 Dec 6	3600	0.6–0.9
IMS J220233+013120	Gemini/GMOS-S	2016 Sep 4–6	2880	1.1–1.3
IMS J220522+025730	Gemini/GMOS-S	2016 Sep 6	1440	1.1
IMS J220635+020136	Gemini/GMOS-S	2018 Jun 18	1440	0.8
IMS J221004+025424	Gemini/GMOS-S	2016 Sep 8	2880	0.5
IMS J221037+024314	Gemini/GMOS-S ^a	2016 Sep 8	9600	0.8
IMS J221118+031207	Gemini/GMOS-S	2016 Sep 4	960	1.2–1.3
Spectroscopically Identified Nonquasars				
IMS J022525–044642	Gemini/GMOS-S	2016 Sep 4–8	5760	1.0
IMS J090540–011038	Gemini/GMOS-N	2018 May 18	1440	0.7

Note.

^a MOS observation with our candidate for a faint quasar at $z \sim 6$ (see details in Section 4.1).

overall flux scale of each spectrum was adjusted using the i -magnitude of each target. In order to increase the S/N, we binned the spectra along the spectral direction by a factor of 2–5 (pixels) by using the inverse-variance weighting method (e.g., Kim et al. 2018). This binning gives the spectral resolution of ~ 300 .

4.2. *Magellan*/IMACS Observation

The optical spectra of the other two candidates were obtained by the Inamori-Magellan Areal Camera and Spectrograph (IMACS; Dressler et al. 2011) on the Magellan Baade 6.5 m Telescope in Las Campanas Observatory, Chile, on 2016 December 3–5. Unlike the Gemini observations, the Magellan spectra were obtained with a standard long-slit mode (not N&S). We used the $f/4$ camera of IMACS with a grating of 150 lines mm^{-1} , giving a spectral resolution of ~ 600 at 7200 \AA for a $0''.9$ slit, and used the OG570 filter to avoid the overlap. This setup gives a wavelength coverage of $5700\text{--}9740 \text{ \AA}$. Note that we used chips 5 and 8 of the $f/4$ camera, which have the highest sensitivities among the IMACS CCD chips. To maximize the S/N, each spectrum was binned by 2×2 during the observation.

For data reduction, we followed general reduction processes: bias subtraction and flat-fielding. After the wavelength calibration with HeNeAr lines, we generated 2D maps of sky lines, by performing a polynomial fitting for pixel values along the spatial direction. We combined the processed 2D spectra from different chips with the astronomical software SWarp (Bertin 2010). Note that there are CCD gaps along the spectral direction, which are located at $\lambda_{\text{obs}} = 6530\text{--}6630 \text{ \AA}$ and $>9700 \text{ \AA}$. Identical to the Gemini spectra, the fluxes within a $1''.0$ diameter aperture were extracted and flux-calibrated using both the spectra of A0V standard stars (HD 18225, HD 85589) and the i -magnitude of each target. The binning was also performed for these spectra in a similar way to that for the Gemini spectra, but the binned spectra have a spectral resolution of ~ 600 .

4.3. Supplemental Spectroscopic Redshift Sample

For some of the medium-band observed objects, we adopted their spectral parameters such as z_{spec} and M_{1450} from the literature. They mainly come from the catalog of $z \sim 5$ quasar candidates by M18, which also used the optical data from CFHTLS to select quasar candidates. Of the 38 quasars they identified with spectroscopy, we used spectral parameters of 18 quasars; they are located in our survey area (IMS) and satisfy our broadband color criteria with the magnitude limit ($i \lesssim 23 \text{ mag}$). Two quasars among them, IMS J221520–000908 and IMS J222216–000406, are also identified by Ikeda et al. (2017), but we took their spectral parameters from M18. Note that we revise the z_{spec} of IMS J140150+514310 from 4.20 in M18 to 5.17 since the $\text{Ly}\alpha$ and $\text{Ly}\beta$ lines are located at 7500 and 6320 \AA , respectively, along with other possible emission lines at the same redshift (see Figure 9 of M18). The M_{1450} value of the quasar is also revised with the z_{spec} . Additionally, we used the spectral parameters of four quasars, which are not included in the final catalog of M18 but spectroscopically identified by them. Consequently, we used the z_{spec} and M_{1450} values of 22 quasars from M18, which are listed in Table 4. Note that there are no M_{1450} values for the four quasars excluded in the final catalog of M18. Including our spectroscopically identified quasars, the total number of spectroscopically identified quasars we used for our study is 35.

5. Results

5.1. Spectroscopic Identification of Quasars

We present the optical spectra of the 15 broadband-selected quasar candidates in Figure 4. Thirteen of them have clear $\text{Ly}\alpha$ breaks at $7000\text{--}7500 \text{ \AA}$ in their spectra, showing that they are high-redshift quasars. Most of the quasars also have strong $\text{Ly}\alpha$ emission line ($\text{S/N} \geq 5$), while IMS J021811–064843 does not. In addition, some spectra show broad emission lines such as C IV (e.g., IMS J085024–041850, IMS J085324–045626, IMS J221037+024314). The quasar spectra we obtained show no significantly unusual feature, except for IMS J221118

Table 4
Quantities of $z \sim 5$ Quasars from the Model Fitting

ID	Photometry				Spectroscopy			References
	z_{phot}	M_{1450} (mag)	α_{λ}	log EW (Å)	z_{spec}	M_{1450} (mag)	log EW (Å)	
IMS J021315–043341	4.70 ^{+0.23} _{-0.10}	-23.7 ^{+0.1} _{-0.2}	-1.8 ^{+0.5} _{-0.9}	0.9 ^{+0.8} _{-0.3}	4.884 ^{+0.003} _{-0.035}	-23.65 ^{+0.73} _{-0.45}	1.9 ^{+0.3} _{-0.3}	(1)
IMS J021523–052946	5.22 ^{+0.17} _{-0.07}	-25.8 ^{+0.1} _{-0.1}	-2.6 ^{+0.4} _{-0.6}	$\lesssim 0.5$	5.13	-25.6	...	(2)
IMS J021811–064843	4.71 ^{+0.04} _{-0.07}	-24.8 ^{+0.1} _{-0.1}	-1.8 ^{+0.5} _{-0.5}	0.9 ^{+0.7} _{-0.3}	4.874 ^{+0.033} _{-0.028}	-24.66 ^{+0.23} _{-0.20}	1.6 ^{+0.2} _{-0.6}	(1)
IMS J022112–034232	4.73 ^{+0.17} _{-0.03}	-24.5 ^{+0.1} _{-0.2}	-1.8 ^{+0.4} _{-0.2}	1.9 ^{+0.2} _{-0.6}	4.976 ^{+0.003} _{-0.003}	-24.27 ^{+0.23} _{-0.14}	2.2 ^{+0.2} _{-0.2}	(1)
IMS J022113–034252	4.74 ^{+0.03} _{-0.01}	-26.4 ^{+0.1} _{-0.1}	-1.8 ^{+0.4} _{-0.2}	1.9 ^{+0.2} _{-0.2}	5.02	-27.0	...	(2)
IMS J085024–041850	4.70 ^{+0.07} _{-0.14}	-24.1 ^{+0.1} _{-0.1}	-2.8 ^{+1.0} _{-0.7}	1.3 ^{+0.4} _{-0.7}	4.799 ^{+0.003} _{-0.003}	-24.18 ^{+0.07} _{-0.08}	2.0 ^{+0.2} _{-0.2}	(1)
IMS J085028–050607	5.20 ^{+0.17} _{-0.04}	-23.9 ^{+0.2} _{-0.1}	-2.4 ^{+1.0} _{-1.1}	1.7 ^{+0.2} _{-0.2}	5.357 ^{+0.003} _{-0.008}	-23.47 ^{+0.22} _{-0.11}	2.2 ^{+0.2} _{-0.2}	(1)
IMS J085225–051413	4.77 ^{+0.20} _{-0.09}	-23.5 ^{+0.2} _{-0.1}	-2.8 ^{+1.0} _{-0.7}	1.1 ^{+0.6} _{-0.5}	4.819 ^{+0.003} _{-0.003}	-23.67 ^{+0.08} _{-0.08}	1.7 ^{+0.2} _{-0.2}	(1)
IMS J085324–045626	4.74 ^{+0.21} _{-0.10}	-23.8 ^{+0.1} _{-0.2}	-2.2 ^{+0.7} _{-0.8}	1.1 ^{+0.6} _{-0.5}	4.832 ^{+0.004} _{-0.004}	-23.89 ^{+0.04} _{-0.05}	1.8 ^{+0.2} _{-0.2}	(1)
IMS J135747+530543	5.20 ^{+0.10} _{-0.03}	-25.5 ^{+0.1} _{-0.1}	-2.0 ^{+0.4} _{-0.5}	1.5 ^{+0.2} _{-0.2}	5.32	-25.5	...	(2)
IMS J135856+514317	4.91 ^{+0.04} _{-0.04}	-25.7 ^{+0.1} _{-0.1}	-2.4 ^{+0.4} _{-0.3}	1.3 ^{+0.2} _{-0.2}	4.97	-25.9	...	(2)
IMS J140147+564145	4.76 ^{+0.06} _{-0.02}	-24.5 ^{+0.1} _{-0.1}	-1.8 ^{+0.2} _{-0.5}	2.1 ^{+0.2} _{-0.2}	4.98	-24.7	...	(2)
IMS J140150+514310	5.16 ^{+0.15} _{-0.01}	-23.4 ^{+0.2} _{-0.1}	-2.0 ^{+0.6} _{-0.9}	1.9 ^{+0.2} _{-0.2}	5.17 ^a	-23.4 ^e	...	(2)
IMS J140440+565651	4.56 ^{+0.09} _{-0.03}	-24.7 ^{+0.1} _{-0.1}	-1.6 ^{+0.4} _{-0.8}	$\lesssim 0.5$	4.74	(2)
IMS J141432+573234	5.14 ^{+0.04} _{-0.07}	-24.8 ^{+0.1} _{-0.1}	-2.4 ^{+0.9} _{-0.8}	1.3 ^{+0.3} _{-0.7}	5.16	-24.7	...	(2)
IMS J142635+543623	4.75 ^{+0.01} _{-0.01}	-26.2 ^{+0.1} _{-0.1}	-2.0 ^{+0.2} _{-0.5}	1.7 ^{+0.2} _{-0.2}	4.76	-26.3	...	(2)
IMS J142854+564602	4.73 ^{+0.27} _{-0.12}	-24.0 ^{+0.1} _{-0.3}	-1.8 ^{+0.5} _{-1.1}	$\lesssim 0.5$	4.73	-24.0	...	(2)
IMS J143156+560201	4.72 ^{+0.04} _{-0.04}	-25.3 ^{+0.1} _{-0.1}	-2.2 ^{+0.7} _{-0.6}	$\lesssim 0.5$	4.75	(2)
IMS J143705+522801	4.83 ^{+0.14} _{-0.11}	-23.8 ^{+0.2} _{-0.1}	-2.4 ^{+0.7} _{-0.5}	1.5 ^{+0.4} _{-0.5}	4.78	(2)
IMS J143757+515115	5.33 ^{+0.12} _{-0.24}	-24.2 ^{+0.3} _{-0.1}	-2.0 ^{+1.0} _{-0.7}	1.5 ^{+0.3} _{-0.9}	5.17	-24.1	...	(2)
IMS J143804+573646	4.83 ^{+0.20} _{-0.20}	-23.5 ^{+0.2} _{-0.2}	$\lesssim -3.6$	0.7 ^{+1.0} _{-0.2}	4.84	-23.5	...	(2)
IMS J143831+563946	4.74 ^{+0.04} _{-0.07}	-24.5 ^{+0.1} _{-0.1}	$\lesssim -3.6$	1.1 ^{+0.5} _{-0.5}	4.82	(2)
IMS J143945+562627	4.70 ^{+0.03} _{-0.06}	-23.4 ^{+0.1} _{-0.1}	-1.4 ^{+0.8} _{-0.8}	1.9 ^{+0.2} _{-0.9}	4.70	-23.2	...	(2)
IMS J220233+013120	5.31 ^{+0.10} _{-0.23}	-24.5 ^{+0.2} _{-0.1}	-2.8 ^{+1.0} _{-0.7}	$\lesssim 0.5$	5.208 ^{+0.022} _{-0.003}	-23.85 ^{+0.10} _{-0.13}	2.0 ^{+0.2} _{-0.2}	(1)
IMS J220522+025730	4.65 ^{+0.07} _{-0.07}	-24.4 ^{+0.1} _{-0.1}	-1.8 ^{+0.5} _{-0.6}	1.3 ^{+0.4} _{-0.7}	4.743 ^{+0.004} _{-0.012}	-24.40 ^{+0.15} _{-0.12}	1.8 ^{+0.2} _{-0.2}	(1)
IMS J220635+020136	5.05 ^{+0.07} _{-0.15}	-24.2 ^{+0.1} _{-0.1}	-1.4 ^{+0.3} _{-0.5}	1.9 ^{+0.2} _{-0.3}	5.101 ^{+0.003} _{-0.003}	-24.41 ^{+0.11} _{-0.08}	1.9 ^{+0.2} _{-0.2}	(1)
IMS J221004+025424	4.55 ^{+0.07} _{-0.05}	-23.6 ^{+0.1} _{-0.1}	-1.2 ^{+0.4} _{-0.7}	1.7 ^{+0.4} _{-0.7}	4.638 ^{+0.003} _{-0.004}	-23.80 ^{+0.06} _{-0.05}	1.8 ^{+0.2} _{-0.2}	(1)
IMS J221037+024314	5.15 ^{+0.07} _{-0.06}	-25.2 ^{+0.1} _{-0.1}	-1.8 ^{+0.6} _{-0.7}	0.9 ^{+0.6} _{-0.3}	5.204 ^{+0.010} _{-0.012}	-25.23 ^{+0.03} _{-0.03}	1.4 ^{+0.2} _{-0.2}	(1)
IMS J221118+031207	4.68 ^{+0.06} _{-0.12}	-24.7 ^{+0.2} _{-0.1}	-1.8 ^{+0.6} _{-0.5}	0.7 ^{+0.8} _{-0.2}	4.821 ^{+0.003} _{-0.003}	-24.42 ^{+0.12} _{-0.13}	2.0 ^{+0.2} _{-0.2}	(1)
IMS J221251–004231	4.76 ^{+0.03} _{-0.01}	-26.0 ^{+0.1} _{-0.1}	-2.6 ^{+0.2} _{-0.3}	1.7 ^{+0.2} _{-0.2}	4.95	-26.3	...	(3)
IMS J221310–002428	4.74 ^{+0.20} _{-0.03}	-23.4 ^{+0.1} _{-0.2}	-1.8 ^{+0.8} _{-0.8}	1.9 ^{+0.3} _{-0.5}	4.80	-23.5	...	(2)
IMS J221520–000908	5.40 ^{+0.06} _{-0.20}	-24.5 ^{+0.1} _{-0.1}	-1.2 ^{+0.5} _{-0.5}	2.1 ^{+0.2} _{-0.2}	5.28	-24.5	...	(2)
IMS J221622+013815	4.87 ^{+0.20} _{-0.12}	-23.4 ^{+0.1} _{-0.2}	-0.8 ^{+0.3} _{-0.7}	1.7 ^{+0.2} _{-0.2}	4.93	-23.3	...	(2)
IMS J221644+001348	4.78 ^{+0.09} _{-0.04}	-25.8 ^{+0.1} _{-0.1}	-1.8 ^{+0.4} _{-0.4}	1.3 ^{+0.3} _{-0.7}	5.01	-25.8	...	(2)
IMS J222216–000406	4.79 ^{+0.24} _{-0.10}	-24.2 ^{+0.2} _{-0.2}	-2.2 ^{+0.5} _{-0.6}	1.5 ^{+0.6} _{-0.9}	4.95	-24.3	...	(2)

Note. The systematic uncertainty of the redshift determination with the Ly α fitting ($\Delta z \lesssim 0.1$; Kim et al. 2015, 2018; M18) is not included in the uncertainties of z_{phot} and z_{spec} . The spectral properties are from (1) this work, (2) M18, and (3) McGreer et al. (2013). For spectroscopic data in this work, we fixed α_{λ} to -1.54 when fitting our quasar SED model (see Section 5.3.3). Note that M_{1450} from (2) and (3) are determined by the i -band magnitudes and z_{spec} , which are matched to model quasar spectra. The difference in cosmological parameters between the literature and this work is also concerned.

^a For IMS J140150+514310, M18 provides $z_{\text{spec}} = 4.20$. However, we revise it to be $z_{\text{spec}} = 5.17$ from the Ly α break in the spectrum shown in Figure 9 of M18 (see details in Section 4.3). M_{1450} is the value that assumes $z_{\text{spec}} = 5.17$.

+031207, which has a seemingly broadened Fe complex at ~ 8000 Å. Out of the 15 candidates we observed, 10 quasars (marked with b in Table 1) are newly discovered ones, and 3 were independently identified by M18. On the other hand, the other 2 candidates selected by broadband color criteria are identified as nonquasar objects (bottom panels of Figure 4), considering that they have no significant break or emission-line feature.

5.2. Medium-band Color Selection and Its Efficiency

In this section, we examine the effectiveness of using medium-band data obtained by SQUEAN for finding $z \sim 5$

quasars. Figure 5 summarizes the numbers of our candidates along the i -band magnitude at various selection or observation stages. There are 70 broadband-selected candidates (gray histogram); 45 of them were observed in three medium bands ($m675$, $m725$, and $m775$; green histogram), and 33 of the 45 candidates satisfy the color criteria (orange histogram) given by Jeon et al. (2016). Among the 33 medium-band-selected candidates, 28 of them have spectroscopic data, and all of them are identified as high-redshift quasars (red histogram). We suggest that the other 5 medium-band-selected candidates are also high-redshift quasars that are bright ($i < 22$ mag) and have high-S/N medium-band data, and yet their SED shape is very much in agreement with the other confirmed quasars. On the

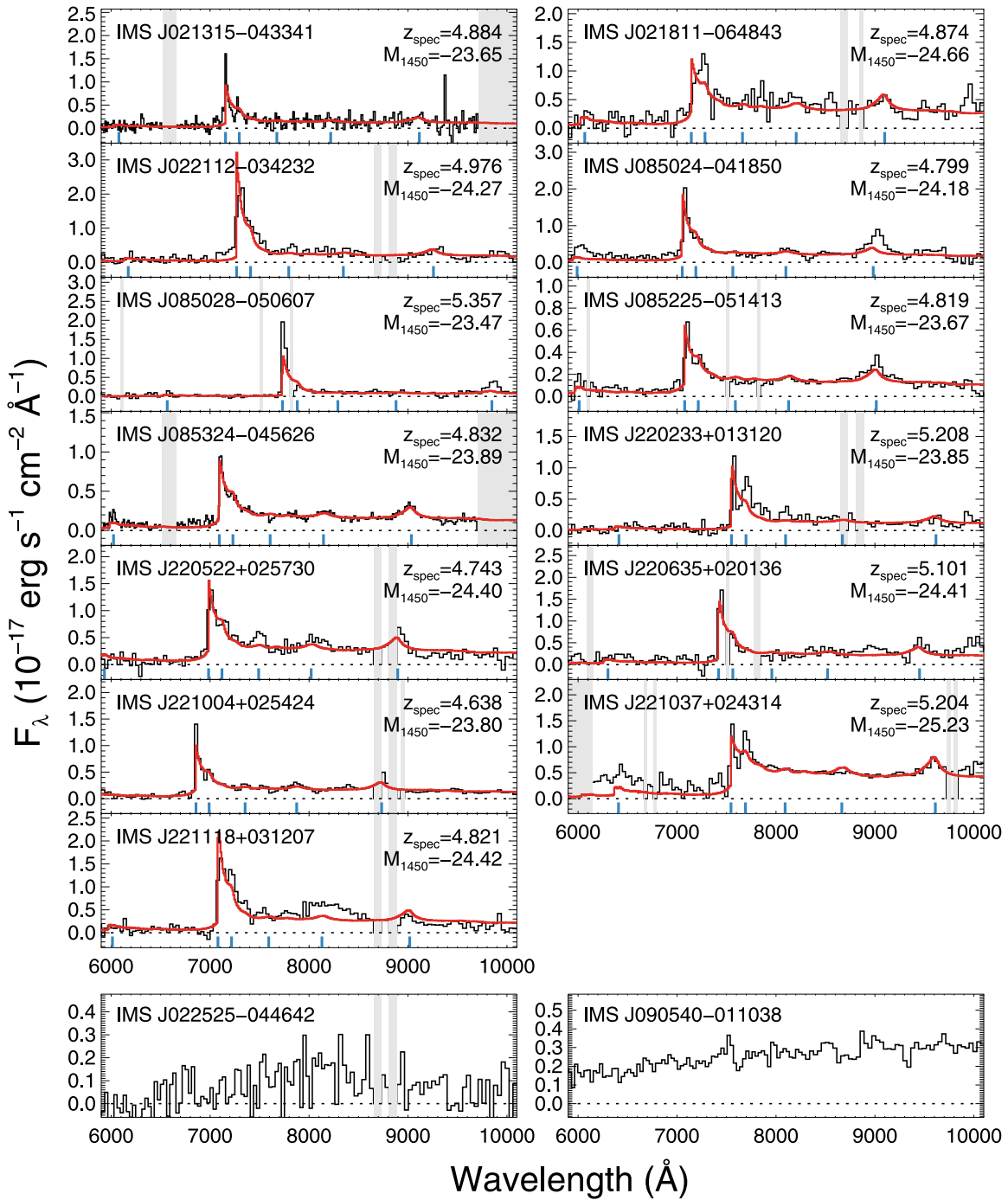


Figure 4. Optical spectra of the identified candidates; the top 13 spectra show the $z \sim 5$ quasars, while the bottom 2 are identified as nonquasar objects. The binned spectra are shown as the black solid lines, while the red solid lines are the best-fit models for each quasar. The blue marks indicate the wavelengths of possible emission lines of each quasar ($\text{Ly}\beta$, $\text{Ly}\alpha$, N V , O I , Si IV , and C IV , from short to long wavelengths). The dotted lines indicate $F_\lambda = 0$, and the shaded regions represent the bad columns (e.g., hot pixels or gap) on CCD or the wavelength range not covered by the observational configuration.

other hand, 27% (12 out of 45) of the broadband-selected candidates were removed by the medium-band color criteria. Out of the 12 excluded candidates, 4 turned out to be quasars. IMS J143945+562627 and IMS J221004+025424 are excluded owing to their redshift ($z \leq 4.7$), so their exclusion is under special circumstances. The other two, IMS J220522+025730 and IMS J220635+020136, are not selected since they have shallow depth images in the $m675$ band, which gives only a lower limit on the $m675-m725$ color. Excluding these two quasars, we estimate that the contaminants occupy 23%

(10 out of 43) of the broadband-selected sample. Note that we assumed that the 10 candidates are all nonquasars or quasars that are out of the explored redshift range. Figure 5 shows the histogram of our candidates for $z \sim 5$ quasars along the i -band magnitude. The medium-band selection becomes more important if we concentrate on faint objects. At $22 < i < 23$, in comparison to $i < 23$, the contamination rate increases to 47% (9 out of 19, except IMS J220635+020136) for the broadband selected candidates that are rejected after the medium-band observation. This is due to the increase of faint red stars that

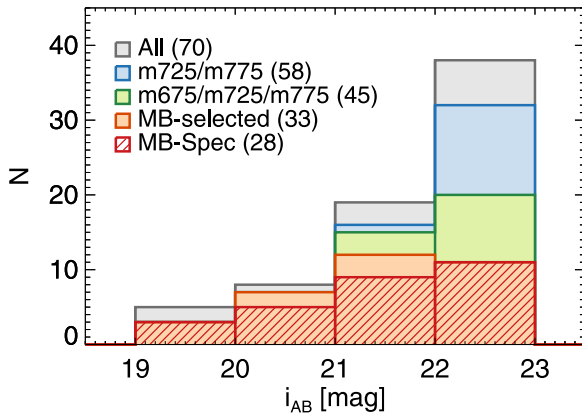


Figure 5. Histogram of our quasar candidates along the i -band magnitude. While the 70 candidates for $z \sim 5$ quasars are shown as the gray histogram, the 58 candidates with $m725$ - and $m775$ -band observations are shown as the blue histogram, and 45 of them also have $m675$ -band photometry (green histogram). Among the medium-band observed candidates, 33 candidates satisfy the medium-band color criteria given by Jeon et al. (2016; orange histogram), and 28 of them were spectroscopically identified as high-redshift quasars by this work and previous works (M18; Ikeda et al. 2017). Note that the 28 candidates are given in the red hatched histogram for easy distinction from the orange histogram. There are seven quasars with spectroscopy, excluded from the red histogram owing to the lack of medium-band observations or the fact that their medium-band colors do not satisfy the color criteria.

can act as interlopers, and without the medium-band approach, the exclusion of such objects becomes more challenging as we go to fainter magnitudes. Consequently, this medium-band approach is an effective way to narrow down the number of plausible candidates for $z \sim 5$ quasars.

However, our method is limited by the broadband selection and photometry. As one can see in Figure 2, there are four quasars at $z \sim 5$ reported by M18 that were excluded from our broadband-selected candidates (purple open diamonds). Except for a quasar with a red $i - z$ color of 1.0, not included in the final catalog of M18, the other three quasars were not selected by our selection criteria because there are small differences in broadband magnitudes (~ 0.1 mag) between M18 and this work. In other words, we may have missed 10% (4 out of 39) of quasars (or candidates) during our broadband selection. We checked whether the photometric accuracy is the main reason for missing 10% of quasars during the broadband selection by using our SED model described in 5.3. We randomly generated 10^5 mock quasars at $4.7 \leq z \leq 5.4$ based on the SED model, controlled by the QLF of M18 with the parameter ranges determined by previous studies (see details in Section 5.3), including photometric uncertainties of 0.1 mag. A total of 11.4% of the mock quasars are rejected by our criteria, corresponding to the fraction of the missed quasars. Thus, to have a highly complete sample, a rather generous broadband selection or a selection from a sample with higher photometry accuracy is desirable before applying the medium-band selection.

5.3. SED Fitting and Redshift Measurements

The estimation of z_{spec} requires spectra with good S/N, which is usually expensive in observing time. As a good alternative, z_{phot} does not require observing time as extensive as spectroscopy, and it is still useful for deriving properties of high-redshift quasars. While z_{phot} of quasars can be determined

by red colors from a sharp break at wavelength shorter than Ly α , their accuracy depends critically on how exactly one can sample the break in multiband photometry. In that regard, medium-band photometry can be useful since its dense wavelength sampling can improve the wavelength estimation of the break. We describe here our derivation of z_{phot} and z_{spec} with a quasar SED model.

5.3.1. Quasar SED Model

We generated an artificial quasar SED model based on the composite spectrum of SDSS quasars (Vanden Berk et al. 2001). Note that there is a more recent composite spectrum of SDSS quasars without the effect of host galaxy contamination (Selsing et al. 2016). But the rest-frame wavelength coverage is only $\lambda_{\text{rest}} > 1000 \text{ \AA}$ for that template ($\lambda_{\text{rest}} > 800 \text{ \AA}$ for Vanden Berk et al. 2001), and the host contamination is not a significant factor at rest-frame UV wavelengths for a quasar with $L_{\text{bol}} \gtrsim 10^{46} \text{ erg s}^{-1}$ (Shen et al. 2011), which is comparable to our quasars. Based on the spectra, we used spectral parameters described below to generate our quasar SED models for fitting.

The quasar continuum slope of the SDSS composite spectrum is $\alpha_\lambda = -1.54$ (Vanden Berk et al. 2001), where $F_\lambda \propto \lambda^{\alpha_\lambda}$. Note that, in a wavelength range of 1450–2200 \AA , α_λ ranges from -2.5 to -0.5 (Davis et al. 2007; Shen et al. 2011; Mazzucchelli et al. 2017). To change the continuum slope of the composite spectrum for a given α_λ , we multiplied a factor of $(\lambda/1000 \text{ \AA})^{\alpha_\lambda - \alpha_{\lambda,0}}$ by the composite spectrum, where $\alpha_{\lambda,0} = -1.54$.

The equivalent width of Ly α and N V $\lambda 1240$ (hereafter EW) is also important to determine the shape of the quasar SED model. For the EW estimation, we integrated the Ly α and N V fluxes over the continuum fluxes at the range of $1160 \leq \lambda_{\text{rest}} (\text{\AA}) \leq 1290$ ($f_{\text{Ly}\alpha+\text{NV}}$). In order to adjust the EW value of the composite spectrum to an arbitrary EW value, we scaled the $f_{\text{Ly}\alpha+\text{NV}}$ at that wavelength range by adjusting the power of p : $f_{\text{Ly}\alpha+\text{NV}} = f_{\text{Ly}\alpha+\text{NV},0} \times (\lambda_{\text{rest}}/1290 \text{ \AA})^p$, where $f_{\text{Ly}\alpha+\text{NV},0}$ is the flux measured from the original spectrum of Vanden Berk et al. (2001).

After adjusting the α_λ and EW, we applied IGM attenuation to the composite spectra, using the polynomial approximation in Madau et al. (1996). The effective optical depth for the Ly α emission line at $4.5 < z < 5.5$ is in line with the values based on several observations (Songaila 2004; Fan et al. 2006) and other simulated templates for $z \sim 5$ quasars (McGreer et al. 2013; M18).

Including M_{1450} as a scaling factor, in summary, four parameters (z , M_{1450} , α_λ , and EW) are used to generate our quasar models for the fitting. Note that the M_{1450} and EW are left as independent parameters for the fitting instead of adopting the Baldwin effect, the correlation between EWs of quasar emission lines and the continuum luminosities (Baldwin 1977), considering the uncertainty of the Baldwin effect for Ly α at high redshift (Constantin et al. 2002; Dietrich et al. 2002). Several quasar model tracks from $z = 4.5$ to 5.5 are shown as the gray dots with solid lines in Figures 2 and 3, where we adopted $M_{1450} = -24$ mag, $\alpha_\lambda = -1.6$, and $\log(\text{EW}/\text{\AA}) = 1.5$. Our simulated models also satisfy the criteria given by McGreer et al. (2013) and Jeon et al. (2016).

5.3.2. Photometric Redshift

Based on the fluxes from the broad- and medium-band observations, z_{phot} was determined by finding the minimum χ^2 value between the observed fluxes and the model fluxes, where χ^2 is defined as

$$\chi^2 = \sum_i \chi_i^2 + \sum_j \chi_j^2. \quad (1)$$

χ_i^2 , the first term, is a standard form of χ^2 for the filters with detection,

$$\chi_i^2 = \left(\frac{f_{o,i} - f_{m,i}}{\sigma_i} \right)^2, \quad (2)$$

where $f_{o,i}$ is the observed flux in the i th band, σ_i is the standard deviation (or uncertainty) of the observed flux, and $f_{m,i}$ is the model flux in the same band, which is calculated by integrating the quasar model fluxes with the weight of the transmission curve of the band. For the case of the filters with the upper limit of fluxes, we refer to the χ^2 derivation by Sawicki (2012), which gives χ_j^2 of the second term of Equation (1),

$$\begin{aligned} \chi_j^2 &= -2 \ln \int_{-\infty}^{f_{\text{lim},j}} \exp \left[-\frac{1}{2} \left(\frac{f_{o,j} - f_{m,j}}{\sigma_j} \right)^2 \right] df \\ &= -2 \ln \left\{ \sqrt{\frac{\pi}{2}} \sigma_j \left[1 + \operatorname{erf} \left(\frac{f_{\text{lim},j} - f_{m,j}}{\sqrt{2} \sigma_j} \right) \right] \right\}, \quad (3) \end{aligned}$$

where $f_{\text{lim},j}$ is the upper limit of the flux in the j th band, $f_{m,j}$ is the model flux in the same band, σ_j is the sensitivity in the same band, and $\operatorname{erf}(x)$ is the error function for the numerical calculation: $\operatorname{erf}(x) = (2/\sqrt{\pi}) \int_0^x e^{-t^2} dt$. Note that we limited the χ_j^2 value by $\chi_j^2 \leq 0$ to restrict the χ^2 value to being negative.

The minimum χ^2 was searched in the following parameter space of z , M_{1450} , α_λ , and EW: $4.5 \leq z \leq 5.5$ with a step size of 0.01, $-27.5 \leq M_{1450}$ (AB mag) ≤ -22.5 with a step size of 0.1 mag, $-3.6 \leq \alpha_\lambda \leq 0.4$ with a step size of 0.2, and $0.5 \leq \log(\text{EW}/\text{\AA}) \leq 2.5$ with a step size of 0.2. Note that the above ranges of α_λ and EW are chosen to cover the α_λ and EW values within about 2σ of the average values for high-redshift quasars, $\alpha_\lambda = -1.6 \pm 1.0$ (Mazzucchelli et al. 2017) and $\log(\text{EW}/\text{\AA}) = 1.542 \pm 0.391$ in the rest frame (Bañados et al. 2016). For each model, we estimated the model flux in each band by calculating the mean flux in each band, which was weighted by the filter transmission curve.

For each quasar, we calculated the χ_{red}^2 value (the reduced χ^2 value, defined as $\chi_{\text{red}}^2 \equiv \chi^2/\nu_{\text{dof}}$, where ν_{dof} is the degree of freedom) for each model with broad (*grizJ*) and existing medium-band (*m675–m825*) fluxes. For the broadband photometry, we gave additional errors on the broadband magnitudes considering the possible variability of quasars between the observing dates of the broad- and medium-band observations.¹⁶

¹⁶ While the CFHTLS and the IMS data were obtained in 2003–2008 and 2009–2013, respectively, the medium-band observations were carried out in 2015–2018, corresponding to a term of 1–2 yr between the observations in the rest frame. The rest-frame far-UV variability of low-redshift quasars over a year scale is $\sim 0.5 \text{ mag yr}^{-1}$ for the most significant variable fraction of $\sim 10\%$ (Welsh et al. 2011). Therefore, we gave an arbitrary error of 0.1 mag ($1\text{--}2 \text{ yr} \times 0.5 \text{ mag yr}^{-1} \times 10\% \sim 0.1 \text{ mag}$) to each broadband magnitude.

We found the minimum χ_{red}^2 value ($\chi_{\text{red},\text{min}}^2$) as the best-fit result and interpolated χ_{red}^2 values in the four parameter spaces to find points of $\chi_{\text{red}}^2 = \chi_{\text{red},\text{min}}^2 + 1$, which are regarded as the marginal points for the errors of each parameter at the 1σ confidence level. Note that the interpolation may over/underestimate the 1σ errors by the bin size, but we expect that the effect is negligible. The best-fit results for 35 spectroscopically identified quasars are listed in Table 4, and Figure 6 shows the SEDs of the quasars with the best-fit models (blue solid lines).

5.3.3. Spectroscopic Redshift (z_{spec})

Similarly to the broad- and medium-band SED fit, z_{spec} and the SED parameters of 13 quasars were also obtained by finding the minimum χ_{red}^2 with Equations (1) and (2), but Equation (3) for the upper limit case is not used. The wavelength range of the fitting was limited to $1100 \leq \lambda_{\text{obs}} (\text{\AA}) / (1 + z_{\text{vis}}) \leq 1600$, where z_{vis} is the redshift determined by visual inspection of the Ly α line on the spectra. It covers the Ly α line and the quasar continuum for the fitting. Among the SED parameters, α_λ was fixed to -1.54 since the wavelength coverage of our spectra is too narrow to reliably estimate the quasar continuum slope. In addition, the adopted parameter grid resolution is higher than the case of z_{phot} when estimating the best-fit parameters and their errors; the step sizes of z_{spec} , M_{1450} , and log EW were pushed down to 0.001, 0.01, and 0.1, respectively. Note that the systematic uncertainty in z_{spec} due to the adopted finite grid size is only $\sim 0.002\text{--}0.004$ for our binned spectra.

In Figure 4, the best-fit models are overplotted with the red lines, and we marked the wavelengths of possible emission lines, such as Ly β $\lambda 1025$, Ly α , N V $\lambda 1240$, O I $\lambda 1304$, Si IV $\lambda 1396$, and C IV $\lambda 1549$, with the blue vertical lines. In addition, the best-fit results are listed in Table 4.

5.3.4. Medium-band Photometric Redshift Accuracy

In Table 4, the best-fit results of our $z \sim 5$ quasar sample are listed. The median uncertainty of z_{spec} is only 0.004, while that of z_{phot} is 0.09. The left panel of Figure 7 shows the comparison of z_{spec} and $z_{\text{phot, BB}}$, the photometric redshift determined with only broadband photometry, for 35 quasars. They show a loose correlation with a linear Pearson correlation coefficient of $r_c = 0.58$. If we introduce the additional medium-band photometry for the z_{phot} determination, there is a tight correlation between z_{spec} and z_{phot} with the improved r_c of 0.90 (right panel of Figure 7). For the two cases, the scatters of normalized median absolute deviations of $|\Delta z|/(1+z)$ (σ_{NMAD}) are 0.029 and 0.016, respectively, where $\Delta z \equiv z_{\text{spec}} - z_{\text{phot}}$ and the z_{spec} are used for the reference redshifts.

Compared to the identical line (the black dashed line), there is a trend of z_{phot} slightly lower than z_{spec} , which is described by the linear relation of $z_{\text{spec}} = 1.087 \times z_{\text{phot}} - 0.506$ (the red solid line in Figure 7). For a simple comparison, we plotted the distribution of $\Delta z/(1+z)$ in Figure 8. The median $\Delta z/(1+z)$ values for z_{phot} (red histogram) and $z_{\text{phot, BB}}$ (blue histogram) are slightly biased toward lower redshift (-0.010 and -0.023 , respectively). The small systematic bias in $\Delta z/(1+z)$ could be explained by the limitation in our quasar models and the filter system. A quasar model with a stronger Ly α emission can give a z_{phot} value that is slightly larger than a model with a weaker Ly α emission since both the models give the same amount of flux within a certain passband that samples the light above the sharp break at Ly α . For

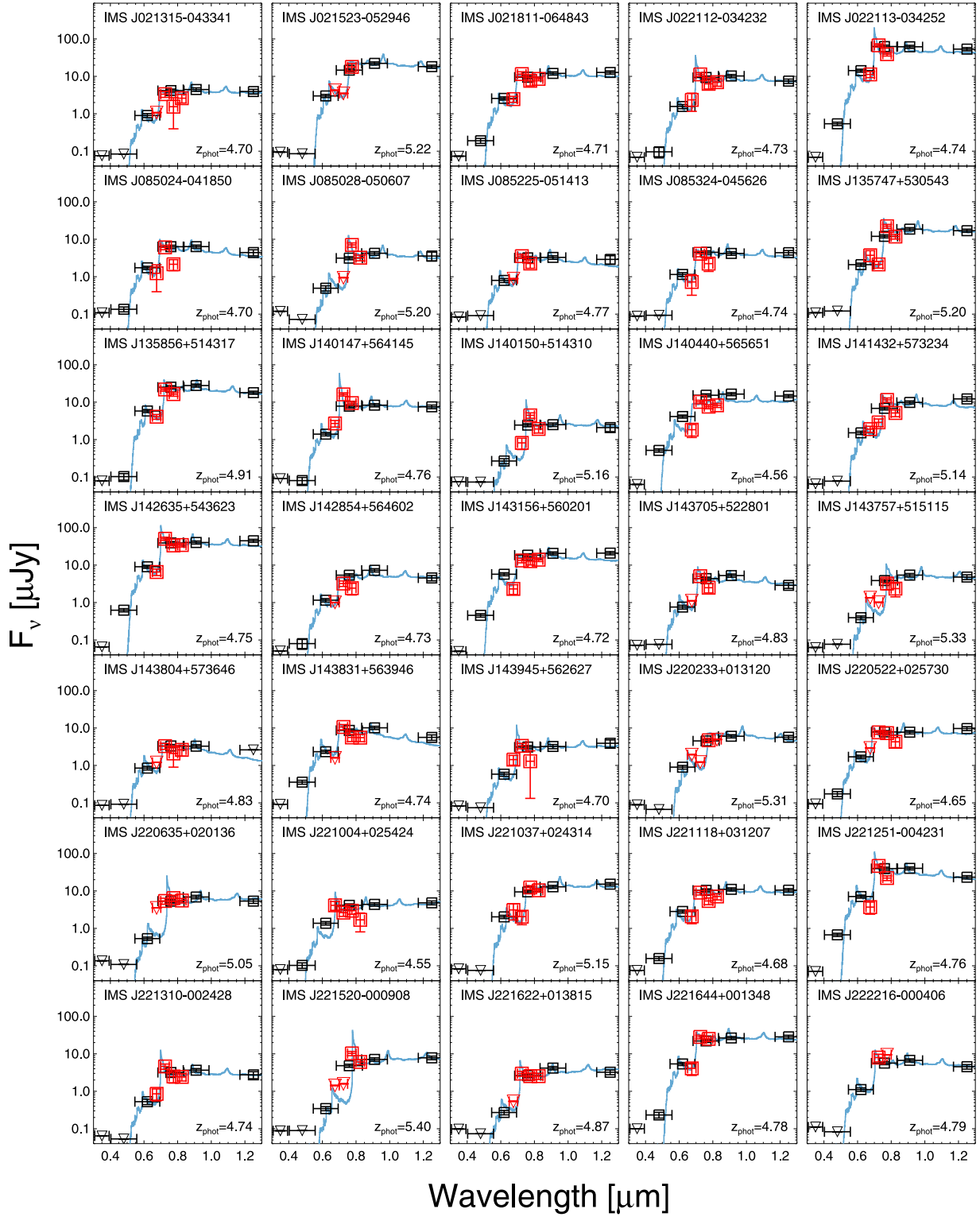


Figure 6. SEDs of quasars with broad- (*ugriz*) and medium-band (*m675–m825*) fluxes, are shown as the black and red squares, respectively. Note that the downward-pointing triangles represent the 2.7σ upper limits. The best-fit model of each quasar is shown with the blue solid line, for which z_{phot} values are also indicated in each panel.

that reason, the z_{phot} probability distribution has a longer tail toward higher redshift. Since we adopt z_{phot} at the maximum probability (the best-fit value), this can result in a slight underestimation in z_{phot} . In addition, the magnitudes at wavelengths longer than $\text{Ly}\alpha$ have smaller uncertainties than the

wavelength below $\text{Ly}\alpha$, and this can lead to a slight underestimation in z_{phot} by giving more weight to the longer-wavelength magnitudes during the model fitting. Then, the fitting procedure tries to fit the longer-wavelength magnitudes better by adjusting the $\text{Ly}\alpha$ strength to preferentially allow a strong $\text{Ly}\alpha$

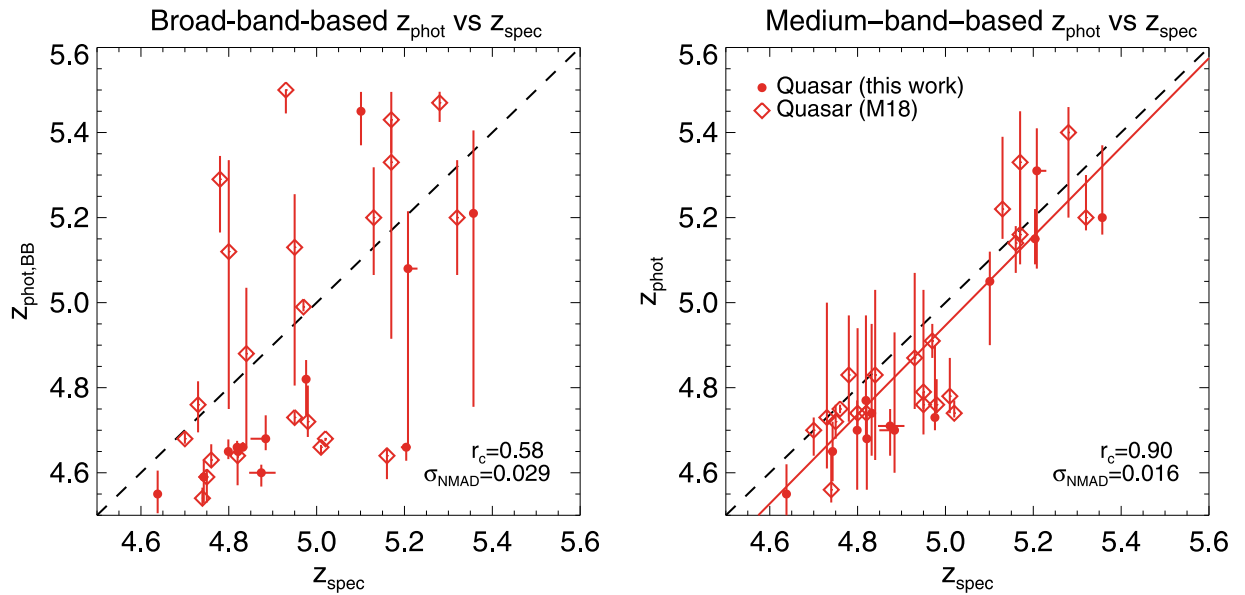


Figure 7. Comparison of z_{phot} vs. z_{spec} of quasars at $z \sim 5$ for the z_{phot} values derived from broadband photometry only (left) and the z_{phot} values from the broad- and medium-band data (right). The symbols are the same as those in Figure 1. The black dotted line shows the case where z_{phot} is identical to z_{spec} , and the red solid line indicates the best-fit result. The Pearson correlation coefficient (r_c) and the scatter of normalized median absolute deviation (σ_{NMAD}) are noted in the lower right corner.

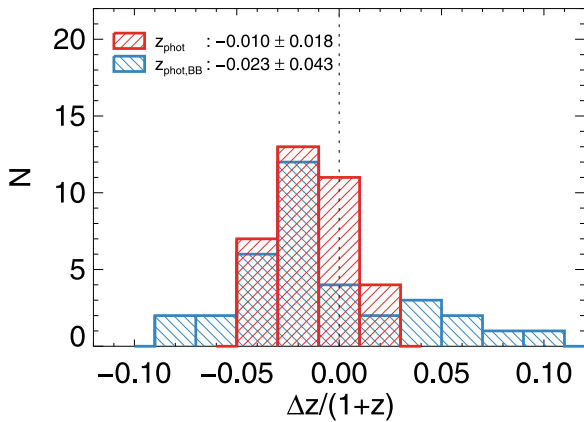


Figure 8. Histogram of $\Delta z/(1+z)$ of $z \sim 5$ quasars, where $\Delta z = z_{\text{phot}} - z_{\text{spec}}$. The red histogram represents the $\Delta z/(1+z)$ distribution based on z_{phot} including the medium-band photometry, while the blue one shows that of $z_{\text{phot, BB}}$ with only the broadband photometry. Their median and standard deviation values are given in the legend. The vertical dotted line indicates $\Delta z/(1+z) = 0$.

emission model with larger z_{phot} values. We confirm this by increasing the photometry accuracy of a filter below Ly α of a $z_{\text{phot}} = 4.7$ quasar from 0.05 to 0.5 mag. When the photometric error increases, the z_{phot} value drops by 0.1. Previous studies of quasar observations in medium bands also support this explanation. Jeon et al. (2016) used similar models that have a sharp break to measure z_{phot} of the bright quasar sample at $4.7 < z < 6.0$ with the SQUEAN medium-band observations, and the $\Delta z/(1+z)$ distribution is a Gaussian distribution of -0.010 ± 0.012 (Jeon et al. 2016). On the other hand, Wolf et al. (2003) used the SDSS quasar spectrum (Vanden Berk et al. 2001) without IGM attenuation for the z_{phot} determination of low-redshift quasars at $0.6 < z < 3.5$ with medium-band observations from the COMBO-17 survey. Their z_{phot} values are almost identical to z_{spec} with uncertainty of $\lesssim 0.05$, corresponding to the low IGM attenuation toward the lower-redshift quasars.

The standard deviation of the z_{phot} case (0.018) is smaller than that of the $z_{\text{phot, BB}}$ case (0.043) by a factor of 2.4, in agreement with the previous suggestion that the z_{phot} determination could be improved with the inclusion of medium-band data. Our z_{phot} estimation method with the medium-band data opens up the possibility of constructing QLFs at redshift bins finer than previous attempts using broadband-based z_{phot} where they constructed QLFs with a coarse bin (e.g., $4.7 < z < 5.4$ in M18).

In summary, using the medium-band data, we can estimate the z_{phot} values of quasars accurately, comparable to the low-resolution spectroscopy. As we described above, the z_{phot} values of high-redshift quasars with $i < 23$ mag determined by the broad- and medium-band data are reasonably matched to z_{spec} by an uncertainty of $\langle |\Delta z|/(1+z) \rangle = 0.016$. Together with the low contamination rate of our medium-band-based approach, a percentage-level z_{phot} accuracy improves the LF and the number density estimation of $z \sim 5$ quasars and can even allow us to trace the large-scale distribution of quasars.

The amount of on-source integration we spent on each object ($i < 23$ mag) was about 2–3 hr. This was for using a 2.1 m telescope under the seeing of $1''.0$ to $1''.5$. In comparison, for the spectroscopic observations with Gemini or Magellan, we invested about 1–2 hr of time per target, including overheads. Considering that 1–2 m class telescope time is much more readily available, the medium-band-based approach is a very cost-effective way to identify high-redshift quasars and measure their redshifts to 1%–2% accuracy.

6. Implication on the QLF at $z \sim 5$

Among the newly discovered 10 quasars, three quasars, IMS J021315–043341, IMS J021811–064843, and IMS J220635+020136, were not reported in the final sample of M18 even as quasar candidates, though these quasars are located in their survey area. The main difference in the broadband selection between ours and M18 is the presence of the NIR data from IMS, so this could be a reason for us picking up new quasars in the area already surveyed by M18. As shown in the middle

panel of Figure 2 and Table 1, however, their *riz* colors (the colors used by M18 for quasar selection) are quite ordinary to be selected as quasar candidates. Also, they are not particularly faint ($i < 22.4$ mag) to be missed owing to large photometry uncertainties. Another possible reason for the rejection is the stellar source classification of M18 by using the difference of PSF-matched magnitude (i_{PSF}) and AUTO magnitudes (i_{AUTO}) in *i* band, $i_{\text{AUTO}} - i_{\text{PSF}} > -0.15$ mag, but the quasars also satisfy this criterion. Overall, the three quasars deserve to be selected by M18 even without the NIR data, but they are not. The differences in photometry between M18 and this work may be the reason, like the four M18 quasars excluded from our candidates (see Section 5.2), but we could not verify this because of the lack of the full catalog of M18 in our hand.

We estimated the chance of finding these quasars from the selection functions from M18. Based on the spectral properties (z , M_{1450} , α_λ , and EW in Table 4), the probabilities of finding the three quasars are as high as $\sim 95\%$, meaning that the quasars are not outliers. We can update the binned QLF of M18 by the three quasars in their sample. Assuming the same photometric (94%) and spectroscopic (86%) completeness of M18 for the three quasars ($21.46 \text{ mag} < i < 22.35 \text{ mag}$), the number counts corrected by the incompleteness (N_{cor} in Table 1 in M18) in the magnitude bins of $M_{1450} = -24.35$ and -23.65 mag increase from 18.0 to 20.6 and from 7.8 to 9.1, respectively, corresponding to the increase in the binned QLF values at the faint end by 15%. This is a modest increase and is consistent with the results from M18 within the error. However, the discovery of the three new quasars in the previously surveyed area suggests the importance of independent surveys and applying different methods to gain a complete sample of high-redshift quasars.

Our results of finding $z \sim 5$ quasars support the scenario of the minor contribution of quasars to the cosmic reionization, as the studies of high-redshift quasars have suggested so far (e.g., Willott et al. 2010; Kashikawa et al. 2015; Kim et al. 2015; Onoue et al. 2017; M18). Several tens of candidates remain to be observed with the medium bands, and the ionizing emissivity by quasars at the faint magnitude range of $M_{1450} \sim -23$ mag could change with our future sample with medium-band observations. However, even if we adopt a pessimistic identification rate of 53% (based on the $22 \text{ mag} < i < 23 \text{ mag}$ quasar sample) for these remaining faint quasar candidates, the expected binned QLF at $z \sim 5$ is marginally in line with the 3σ upper limit by M18, meaning that faint quasars contribute to a minor fraction of UV photons to ionize IGM. The gap in the $z \sim 5$ quasar number density between optical and X-ray surveys would still remain unsolved.

7. Summary

We have performed a $z \sim 5$ quasar survey with a medium-band-based approach to improve faint quasar candidate selection based on the broadband colors. The follow-up imaging and spectroscopy allow us to find 10 new quasars at $z \sim 5$, among which 3 were missed in the surveys covering the same area. Using medium-band data of 35 spectroscopically identified quasars, we demonstrate that quasars can be distinguished effectively from other objects (e.g., brown dwarfs, galaxies) by imposing medium-band selection criteria on the broadband-selected candidates ($\gtrsim 20\%$ of the broadband-selected sample is ruled out). Furthermore, with the inclusion of the medium-band data, the z_{phot} accuracy improves by a

factor of 2–3 in comparison to $z_{\text{phot, BB}}$, producing a nearly 1% level accuracy of $\langle |\Delta z| / (1 + z) \rangle = 0.016$ (or $\sigma_{\text{NMAD}} = 0.016$). Despite our discovery of new faint quasars, the scarcity of $z \sim 5$ quasars is consistent with the recent suggestions that the high-redshift quasars are not main contributors to the cosmic reionization in the early universe. Based on the high accuracy of the z_{phot} determination, we expect that the completion of the medium-band survey will enable us to improve the constraint on the faint-end slope of the QLF at $z \sim 5$ in the near future.

This work was supported by the National Research Foundation of Korea (NRF), grant No. 2017R1A3A3001362, funded by the Korea government (MSIP). This work was supported by the K-GMT Science Program (PID:GS-2016B-Q-11, GS-2016B-Q-46, GS-2017A-Q-19, GS-2018A-Q-220, and GN-2018A-Q-315) of the Korea Astronomy and Space Science Institute (KASI). Based on observations obtained with MegaPrime/MegaCam, a joint project of CFHT and CEA/IRFU, at the Canada–France–Hawaii Telescope (CFHT), which is operated by the National Research Council (NRC) of Canada, the Institut National de Science de l’Univers of the Centre National de la Recherche Scientifique (CNRS) of France, and the University of Hawaii. This work is based in part on data products produced at Terapix available at the Canadian Astronomy Data Centre as part of the Canada–France–Hawaii Telescope Legacy Survey, a collaborative project of NRC and CNRS. The United Kingdom Infrared Telescope (UKIRT) is supported by NASA and operated under an agreement among the University of Hawaii, the University of Arizona, and the Lockheed Martin Advanced Technology Center; operations are enabled through the cooperation of the Joint Astronomy Centre of the Science and Technology Facilities Council of the U.K. Based on observations obtained at the Gemini Observatory acquired through the Gemini Science Archive and processed using the Gemini IRAF package, which is operated by the Association of Universities for Research in Astronomy, Inc., under a cooperative agreement with the NSF on behalf of the Gemini partnership: the National Science Foundation (United States), the National Research Council (Canada), CONICYT (Chile), the Australian Research Council (Australia), Ministério da Ciência, Tecnologia e Inovação (Brazil), and Ministerio de Ciencia, Tecnología e Innovación Productiva (Argentina). This paper includes data gathered with the 6.5 m Magellan Telescopes located at Las Campanas Observatory, Chile. This research was supported by the Basic Science Research Program through the National Research Foundation of Korea (NRF) funded by the Ministry of Education (NRF-2017R1A6A3A04005158). This paper includes data taken at the McDonald Observatory of the University of Texas at Austin.

Facilities: UKIRT (WFCAM), Struve (SQUEAN), Magellan: Baade (IMACS), Gemini:South (GMOS-S), Gemini:Gillett (GMOS-N), CFHT (MegaCam), Sloan.

Software: SExtractor (Bertin & Arnouts 1996), SWarp (Bertin 2010).

Appendix A Correction for the Broadband Colors

In this section, we describe how we calculate the color offsets of each CFHTLS tile to improve the color selection in this work. We used the median stellar loci of 0.3 million SDSS -2MASS stars of Covey et al. (2007) as a reference. Though their colors are not corrected for the Galactic extinction, the

Table 5
Color Offsets of Spectroscopically Identified Candidates for $z \sim 5$ Quasars

ID	C_{g-r}^{offset} (mag)	C_{r-i}^{offset} (mag)	C_{i-z}^{offset} (mag)	C_{i-J}^{offset} (mag)
Spectroscopically Identified Quasars				
IMS J021315–043341	–0.05	–0.01	–0.08	0.20
IMS J021523–052946	–0.02	0.02	–0.06	0.21
IMS J021811–064843	–0.04	–0.01	–0.15	0.12
IMS J022112–034232	–0.04	–0.01	–0.09	0.21
IMS J022113–034252	–0.04	–0.01	–0.09	0.21
IMS J085024–041850	–0.03	0.03	–0.05	0.13
IMS J085028–050607	–0.02	0.04	0.02	0.11
IMS J085225–051413	0.00	0.03	0.02	0.11
IMS J085324–045626	0.00	0.03	0.02	0.11
IMS J135747+530543	0.03	–0.04	–0.02	0.19
IMS J135856+514317	–0.04	0.06	–0.06	0.23
IMS J140147+564145	–0.01	0.06	–0.10	0.16
IMS J140150+514310	–0.04	0.06	–0.06	0.23
IMS J140440+565651	–0.02	0.07	–0.03	0.17
IMS J141432+573234	0.04	0.02	–0.04	0.21
IMS J142635+543623	0.01	0.01	–0.10	0.12
IMS J142854+564602	–0.01	0.00	–0.08	0.23
IMS J143156+560201	–0.01	0.00	–0.08	0.23
IMS J143705+522801	0.00	0.01	–0.08	0.23
IMS J143757+515115	–0.03	–0.03	–0.04	0.20
IMS J143804+573646	0.00	0.01	–0.01	0.26
IMS J143831+563946	0.02	–0.07	–0.02	0.27
IMS J143945+562627	0.02	–0.07	–0.02	0.27
IMS J220233+013120	–0.05	–0.03	–0.09	0.18
IMS J220522+025730	–0.05	–0.04	–0.12	0.09
IMS J220635+020136	0.02	–0.01	–0.13	0.12
IMS J221004+025424	–0.02	0.03	0.03	0.13
IMS J221037+024314	–0.02	0.03	0.03	0.13
IMS J221118+031207	–0.02	0.03	0.03	0.13
IMS J221251–004231	–0.10	–0.01	–0.09	0.16
IMS J221310–002428	–0.10	–0.01	–0.09	0.16
IMS J221520–000908	–0.04	–0.15	0.04	0.17
IMS J221622+013815	–0.04	–0.01	–0.09	0.14
IMS J221644+001348	–0.04	–0.07	–0.10	0.12
IMS J222216–000406	–0.04	–0.05	–0.11	0.12
Spectroscopically Identified Nonquasars				
IMS J022525–044642	0.00	0.05	–0.10	0.22
IMS J090540–011038	0.00	–0.02	–0.10	0.15

shape of the loci is consistent with the recent loci based on the 1 million SDSS–2MASS–WISE stars with a low extinction of $A_r < 0.125$ (Davenport et al. 2014). Furthermore, the loci of Covey et al. (2007) are also in line with those of Gwyn (2012) based on the point sources in CFHTLS data. Note that we used the loci of Covey et al. (2007), instead of those of Davenport et al. (2014), which used larger color bins in extreme cases

(e.g., $r-i > 2$). For the objects classified as stars ($\text{CLASS_STAR} > 0.95$ from SExtractor) within the magnitude range of $17 < r < 21$ in each CFHTLS tile, we estimated the color offsets C_k^{offset} (where the index k indicates the color: $g-r$, $r-i$, $i-z$, and $i-J$), which minimize the color distance factor D_{color} , given as

$$(D_{\text{color}})^2 = \sum_i \sum_k \frac{(X_{i,k}^{\text{obj}} - X_{i,k}^{\text{locus}} + C_k^{\text{offset}})^2}{(\sigma_{i,k}^{\text{obj}})^2 + (\sigma_{i,k}^{\text{locus}})^2}, \quad (4)$$

where $X_{i,k}^{\text{obj}}$ is the k color value of the i th object, $X_{i,k}^{\text{locus}}$ is the k color value of the nearest stellar locus of Covey et al. (2007) to $X_{i,k}^{\text{obj}}$, $\sigma_{i,k}^{\text{locus}}$ is the quadratic sum of magnitude errors consisting of the k color of the i th object, and $\sigma_{i,k}^{\text{locus}}$ is the given error of $X_{i,k}^{\text{locus}}$ by Covey et al. (2007). For the whole survey area, the mean values of C_k^{offset} are less than 0.2 mag with small standard deviations of ~ 0.05 mag: $C_{g-r}^{\text{offset}} = -0.02 \pm 0.05$, $C_{r-i}^{\text{offset}} = -0.01 \pm 0.05$, $C_{i-z}^{\text{offset}} = -0.07 \pm 0.06$, and $C_{i-J}^{\text{offset}} = 0.18 \pm 0.04$. The C_{i-J}^{offset} are much larger than the other C_k^{offset} on average, indicating that the J -band magnitudes might be slightly over-estimated when we introduce the bright 2MASS stars for the z p estimation of IMS data. We list the C_k^{offset} values of our candidates with spectroscopy data in Table 5.

Appendix B Spectra of Nonquasar Objects

As we described in Section 2.1, spectroscopic data were obtained for some of the broadband-selected quasar candidates before we improved our photometry. Later, these were excluded from quasar candidates based on the improved broadband photometry. Not surprisingly, these objects were spectroscopically identified as nonquasars. This section provides spectra of these nonquasar objects. The spectroscopic observations of these objects were carried out with GMOS on the Gemini-North/South 8 m Telescopes (PID:GS-2016B-Q-46, GS-2017A-Q-19, and GN-2018A-Q-315) and IMACS on the Magellan Baade 6.5 m Telescope. The information of the observing runs and their i -band magnitudes are listed in Table 6, and Figure 9 shows their optical spectra. These candidates are identified as nonquasar objects without any break or line feature at $\gtrsim 7000 \text{ \AA}$ as we saw for our newly discovered quasars. The spectra obtained with IMACS show increased fluxes at $\sim 6600 \text{ \AA}$ since it is close to the CCD gap. However, there is a significant continuum emission at $\lambda_{\text{obs}} < 6500 \text{ \AA}$ with no emission-line features in both the 1D and the 2D spectra. Therefore, these objects are regarded as nonquasar objects.

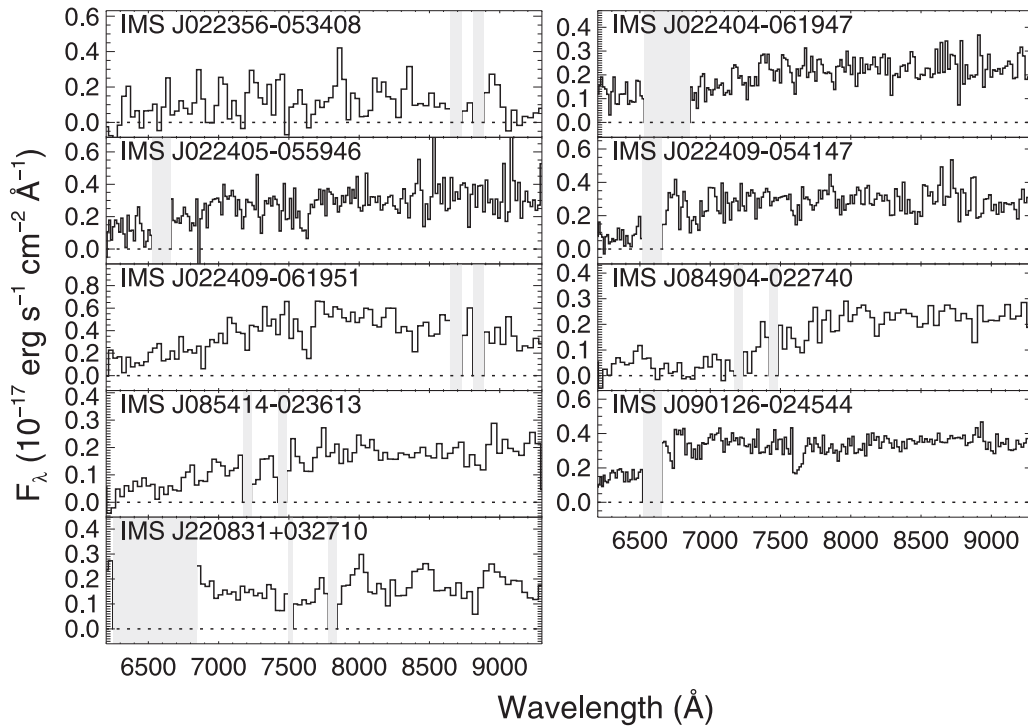


Figure 9. Optical spectra of nonquasar objects. The binned spectra are shown as black solid lines. The dotted lines indicate $F_\lambda = 0$, and the shaded regions represent the bad column area on the CCD.

Table 6
Spectroscopic Observations of Nonquasar Objects

ID	Telescope/Instrument	Date	Exposure Time (s)	i (mag)
IMS J022356–053408	Gemini/GMOS-S	2016 Sep 3–4	5760	22.79
IMS J022404–061947	Magellan/IMACS	2016 Dec 5	3600	22.41
IMS J022405–055946	Magellan/IMACS	2016 Dec 6	1800	22.09
IMS J022409–054147	Magellan/IMACS	2016 Dec 6	1800	22.05
IMS J022409–061951	Gemini/GMOS-S	2016 Sep 3	960	21.56
IMS J084904–022740	Gemini/GMOS-S	2017 Feb 22	4800	22.71
IMS J085414–023613	Gemini/GMOS-S	2017 Feb 22	4800	22.76
IMS J090126–024544	Magellan/IMACS	2016 Dec 6	2100	21.91
IMS J220831+032710	Gemini/GMOS-S	2018 Jun 22	3000	22.84

Note. These objects were selected before the improved photometry described in Section 2.1.

ORCID iDs

Yongjung Kim <https://orcid.org/0000-0003-1647-3286>
 Myungshin Im <https://orcid.org/0000-0002-8537-6714>
 Yiseul Jeon <https://orcid.org/0000-0003-4847-7492>
 Minjin Kim <https://orcid.org/0000-0002-3560-0781>
 Soojong Pak <https://orcid.org/0000-0002-2548-238X>
 Hyunsung David Jun <https://orcid.org/0000-0003-1470-5901>
 Marios Karouzos <https://orcid.org/0000-0002-8858-3188>
 Dohyeong Kim <https://orcid.org/0000-0002-6925-4821>
 Duho Kim <https://orcid.org/0000-0001-5120-0158>
 Jae-Woo Kim <https://orcid.org/0000-0002-1710-4442>
 Ji Hoon Kim <https://orcid.org/0000-0002-1418-3309>
 Seong-Kook Lee <https://orcid.org/0000-0001-5342-8906>

References

- Baldwin, J. A. 1977, *ApJ*, 214, 679
 Bañados, E., Venemans, B. P., Decarli, R., et al. 2016, *ApJS*, 227, 11
 Bañados, E., Venemans, B. P., Mazzucchelli, C., et al. 2018, *Natur*, 553, 473
 Bañados, E., Venemans, B. P., Morganson, E., et al. 2014, *AJ*, 148, 14
 Bertin, E. 2010, SWarp: Resampling and Co-adding FITS Images Together, Astrophysics Source Code Library, ascl:1010.068
 Bertin, E., & Arnouts, S. 1996, *A&AS*, 117, 393
 Bouwens, R. J., Oesch, P. A., Illingworth, G. D., Ellis, R. S., & Stefanon, M. 2017, *ApJ*, 843, 129
 Burrows, A., Sudarsky, D., & Hubeny, I. 2006, *ApJ*, 640, 1063
 Cardelli, J. A., Clayton, G. C., & Mathis, J. S. 1989, *ApJ*, 345, 245
 Choi, N., Park, W.-K., Lee, H.-I., et al. 2015, *JKAS*, 48, 177
 Constantin, A., Shields, J. C., Hamann, F., Foltz, C. B., & Chaffee, F. H. 2002, *ApJ*, 565, 50
 Covey, K. R., Ivezić, Ž., Schlegel, D., et al. 2007, *AJ*, 134, 2398
 Davenport, J. R. A., Ivezić, Ž., Becker, A. C., et al. 2014, *MNRAS*, 440, 3430
 Davis, S. W., Woo, J.-H., & Blaes, O. M. 2007, *ApJ*, 668, 682
 Dayal, P., & Ferrara, A. 2018, *PhR*, 780, 1
 Dietrich, M., Hamann, F., Shields, J. C., et al. 2002, *ApJ*, 581, 912
 Dressler, A., Bigelow, B., Hare, T., et al. 2011, *PASP*, 123, 288
 Fan, X., Narayanan, V. K., Lupton, R. H., et al. 2001, *AJ*, 122, 2833
 Fan, X., Strauss, M. A., Becker, R. H., et al. 2006, *AJ*, 132, 117
 Fontanot, F., Cristiani, S., Monaco, P., et al. 2007, *A&A*, 461, 39

- Fontanot, F., Cristiani, S., Pfrommer, C., Cupani, G., & Vanzella, E. 2014, *MNRAS*, **438**, 2097
- Fontanot, F., Cristiani, S., & Vanzella, E. 2012, *MNRAS*, **425**, 1413
- Gallerani, S., Fan, X., Maiolino, R., & Pacucci, F. 2017, *PASA*, in press (doi:10.1017/pasa.2017.14)
- Gawiser, E., van Dokkum, P. G., Herrera, D., et al. 2006, *ApJS*, **162**, 1
- Giallongo, E., Grazian, A., Fiore, F., et al. 2015, *A&A*, **578**, A83
- Grazian, A., Giallongo, E., Paris, D., et al. 2017, *A&A*, **602**, A18
- Gunn, J. E., & Stryker, L. L. 1983, *ApJS*, **52**, 121
- Gwyn, S. D. J. 2012, *AJ*, **143**, 38
- Haardt, F., & Madau, P. 2012, *ApJ*, **746**, 125
- Hassan, S., Davé, R., Mitra, S., et al. 2018, *MNRAS*, **473**, 227
- Hewett, P. C., Warren, S. J., Leggett, S. K., & Hodgkin, S. T. 2006, *MNRAS*, **367**, 454
- Hook, I. M., Jørgensen, I., Allington-Smith, J. R., et al. 2004, *PASP*, **116**, 425
- Hudelot, P., Cuillandre, J.-C., Withington, K., et al. 2012, *yCat*, **2317**
- Ikeda, H., Nagao, T., Matsuoka, K., et al. 2012, *ApJ*, **756**, 160
- Ikeda, H., Nagao, T., Matsuoka, K., et al. 2017, *ApJ*, **846**, 57
- Im, M., Griffiths, R. E., & Ratnatunga, K. U. 1997, *ApJ*, **475**, 457
- Japelj, J., Vanzella, E., Fontanot, F., et al. 2017, *MNRAS*, **468**, 389
- Jeon, Y., Im, M., Ibrahimov, M., et al. 2010, *ApJS*, **190**, 166
- Jeon, Y., Im, M., Kim, D., et al. 2017, *ApJS*, **231**, 16
- Jeon, Y., Im, M., Pak, S., et al. 2016, *JKAS*, **49**, 25
- Jiang, L., McGreer, I. D., Fan, X., et al. 2016, *ApJ*, **833**, 222
- Jun, H. D., Im, M., Lee, H. M., et al. 2015, *ApJ*, **806**, 109
- Kashikawa, N., Ishizaki, Y., Willott, C. J., et al. 2015, *ApJ*, **798**, 28
- Kim, E., Park, W.-K., Jeong, H., et al. 2011, *JKAS*, **44**, 115
- Kim, S., Jeon, Y., Lee, H.-I., et al. 2016, *PASP*, **128**, 115004
- Kim, Y., Im, M., Jeon, Y., et al. 2015, *ApJL*, **813**, L35
- Kim, Y., Im, M., Jeon, Y., et al. 2018, *ApJ*, **855**, 138
- Lawrence, A., Warren, S. J., Almaini, O., et al. 2007, *MNRAS*, **379**, 1599
- Lim, J., Chang, S., Pak, S., et al. 2013, *JKAS*, **46**, 161
- Madau, P., Ferguson, H. C., Dickinson, M. E., et al. 1996, *MNRAS*, **283**, 1388
- Madau, P., & Haardt, F. 2015, *ApJL*, **813**, L8
- Matsuoka, Y., Onoue, M., Kashikawa, N., et al. 2016, *ApJ*, **828**, 26
- Matsuoka, Y., Onoue, M., Kashikawa, N., et al. 2017, *PASJ*, **70**, 35
- Matthee, J., Sobral, D., Best, P., et al. 2017, *MNRAS*, **465**, 3637
- Matute, I., Márquez, I., Masegosa, J., et al. 2012, *A&A*, **542**, A20
- Matute, I., Masegosa, J., Márquez, I., et al. 2013, *A&A*, **557**, A78
- Mazzucchelli, C., Bañados, E., Venemans, B. P., et al. 2017, *ApJ*, **849**, 91
- McGreer, I. D., Fan, X., Jiang, L., & Cai, Z. 2018, *AJ*, **155**, 131
- McGreer, I. D., Jiang, L., Fan, X., et al. 2013, *ApJ*, **768**, 105
- Moles, M., Benítez, N., Aguerri, J. A. L., et al. 2008, *AJ*, **136**, 1325
- Mortlock, D. J., Warren, S. J., Venemans, B. P., et al. 2011, *Natur*, **474**, 616
- Onoue, M., Kashikawa, N., Willott, C. J., et al. 2017, *ApJL*, **847**, L15
- Pâris, I., Petitjean, P., Ross, N. P., et al. 2017, *A&A*, **597**, A79
- Park, W.-K., Pak, S., Im, M., et al. 2012, *PASP*, **124**, 839
- Parsa, S., Dunlop, J. S., & McLure, R. J. 2018, *MNRAS*, **474**, 2904
- Pickles, A. J. 1998, *PASP*, **110**, 863
- Planck Collaboration, Adam, R., Aghanim, N., et al. 2016, *A&A*, **596**, A108
- Reed, S. L., McMahon, R. G., Martini, P., et al. 2017, *MNRAS*, **468**, 4702
- Ricci, F., Marchesi, S., Shankar, F., La Franca, F., & Civano, F. 2017, *MNRAS*, **465**, 1915
- Richards, G. T., Strauss, M. A., Fan, X., et al. 2006, *AJ*, **131**, 2766
- Robertson, B. E., Ellis, R. S., Furlanetto, S. R., & Dunlop, J. S. 2015, *ApJL*, **802**, L19
- Robertson, B. E., Furlanetto, S. R., Schneider, E., et al. 2013, *ApJ*, **768**, 71
- Sawicki, M. 2012, *PASP*, **124**, 1208
- Schlafly, E. F., & Finkbeiner, D. P. 2011, *ApJ*, **737**, 103
- Selsing, J., Fynbo, J. P. U., Christensen, L., & Krogager, J.-K. 2016, *A&A*, **585**, A87
- Shen, Y., Richards, G. T., Strauss, M. A., et al. 2011, *ApJS*, **194**, 45
- Skrutskie, M. F., Cutri, R. M., Stiening, R., et al. 2006, *AJ*, **131**, 1163
- Songaila, A. 2004, *AJ*, **127**, 2598
- van Dokkum, P. G., Labbé, I., Marchesini, D., et al. 2009, *PASP*, **121**, 2
- Vanden Berk, D. E., Richards, G. T., Bauer, A., et al. 2001, *AJ*, **122**, 549
- Venemans, B. P., Bañados, E., Decarli, R., et al. 2015a, *ApJL*, **801**, L11
- Venemans, B. P., Findlay, J. R., Sutherland, W. J., et al. 2013, *ApJ*, **779**, 24
- Venemans, B. P., Verdoes Kleijn, G. A., Mwebaze, J., et al. 2015b, *MNRAS*, **453**, 2259
- Wang, F., Wu, X.-B., Fan, X., et al. 2016, *ApJ*, **819**, 24
- Welsh, B. Y., Wheatley, J. M., & Neil, J. D. 2011, *A&A*, **527**, A15
- Willott, C. J., Delorme, P., Reylé, C., et al. 2010, *AJ*, **139**, 906
- Wolf, C., Wisotzki, L., Borch, A., et al. 2003, *A&A*, **408**, 499
- Wu, X.-B., Wang, F., Fan, X., et al. 2015, *Natur*, **518**, 512
- Yang, J., Fan, X., Wu, X.-B., et al. 2017, *AJ*, **153**, 184
- Yang, J., Wang, F., Wu, X.-B., et al. 2016, *ApJ*, **829**, 33